

Article

Error Evolutions and Analyses on Joint Effects of SST and SL via Intermediate Coupled Models and Conditional Nonlinear Optimal Perturbation Method

Bin Mu, Xiaoyun Qin, Shijin Yuan * and Bo Qin 

School of Software Engineering, Tongji University, Shanghai 201804, China; binmu@tongji.edu.cn (B.M.); 1911040@tongji.edu.cn (X.Q.); 1710966@tongji.edu.cn (B.Q.)

* Correspondence: yuanshijin@tongji.edu.cn

Abstract: A seasonal predictability barrier has long been noticed in ENSO forecasting with numerical models. Previous studies explored the impact of seasonal optimal initial perturbation evolutions in sea surface temperature anomalies (SSTA) on ENSO forecasting using the intermediate coupled model (ICM) via the conditional nonlinear optimal perturbation (CNOP) method. In this paper, we investigate the joint effects of SSTA and sea level anomalies (SLA) from the perspective of the optimal growth initial error (OGE). After determining the four seasonal OGEs about SSTA and SLA (i.e., SSTA-OGE, SLA-OGE and Joint-OGE), we first demonstrate the patterns, evolutions and the resulting spring predictability barrier (SPB) of the above OGEs. Then, we analyze the mechanism of OGE evolutions and SPB. Finally, we conduct observing system simulation experiments to determine the best (economic) observation network. Our experimental results indicate that the ENSO evolution error induced by SSTA-OGE and Joint-OGE presents season dependency, but SLA-OGE has no impact on ENSO evolution. Moreover, Joint-OGEs induce error evolutions and the SPB with more significant intensity than SSTA-OGEs and SLA-OGEs. From mechanism analyses, the evolutions of SSTA-OGEs are mainly dominated by Bjerknes feedback. Further, the evolution dynamics of Joint-OGEs primarily contain the continuous heating between the upper ocean combined with Bjerknes feedback and thermal diffusion in response to the discharge process. In addition, comprehensive and economical sensitive areas are identified through Joint-OGE, including the central-eastern equatorial Pacific and the western and north-eastern tropical Pacific boundary, which contribute to the ENSO prediction benefits reaching 58.31% on average.

Keywords: ENSO; joint effects; predictability barrier; seasonal OGE; CNOP; target observation sensitive area



Citation: Mu, B.; Qin, X.; Yuan, S.; Qin, B. Error Evolutions and Analyses on Joint Effects of SST and SL via Intermediate Coupled Models and Conditional Nonlinear Optimal Perturbation Method. *J. Mar. Sci. Eng.* **2023**, *11*, 910. <https://doi.org/10.3390/jmse11050910>

Academic Editor: Jinyu Sheng

Received: 24 March 2023

Revised: 20 April 2023

Accepted: 20 April 2023

Published: 24 April 2023



Copyright: © 2023 by the authors. Licensee MDPI, Basel, Switzerland. This article is an open access article distributed under the terms and conditions of the Creative Commons Attribution (CC BY) license (<https://creativecommons.org/licenses/by/4.0/>).

1. Introduction

The El Niño–Southern Oscillation (ENSO), the most prominent year-to-year climate variation on Earth, occurs irregularly every 2–7 years in the equatorial Pacific Ocean [1]. The origins and development of ENSO have an enormous impact on the global climate and economy [2]. Thus, the accurate forecasting and understanding of this phenomenon are crucial for meteorological researchers worldwide. The marine aspect of the ENSO can be characterized by two main opposite states: El Niño events defined by positive sea surface temperature anomalies (SSTAs) in the equatorial Pacific Ocean and La Niña events marked by negative SSTA in the same region [3].

In the late 20th century, numerical models were able to effectively predict ENSO events with lead times of 6 to 12 months [4]. Even though such progress was achieved, the ENSO prediction still has great uncertainties [5]. For example, Figure 1, provided by the IRI/CPC [6], including 17 dynamic models and 7 statistical models, shows forecast results in the Niño3.4 index, which are widely divergent from the observations reaching roughly 3 °C. The primary reason is that numerical models are often established based on the

air–sea coupling model in a certain period [7]. As a result, the limited dynamics lead to a decrease in ENSO forecasting skill. Typically, most numerical models display significant declines in ENSO prediction skill across the boreal spring, i.e., spring predictability barrier (SPB). As shown in Figure 1, the prediction divergence even exceeds 4 °C in spring, marked by two blue rectangles. It also points out that the SPB phenomenon has a more serious impact on ENSO forecasting [8].

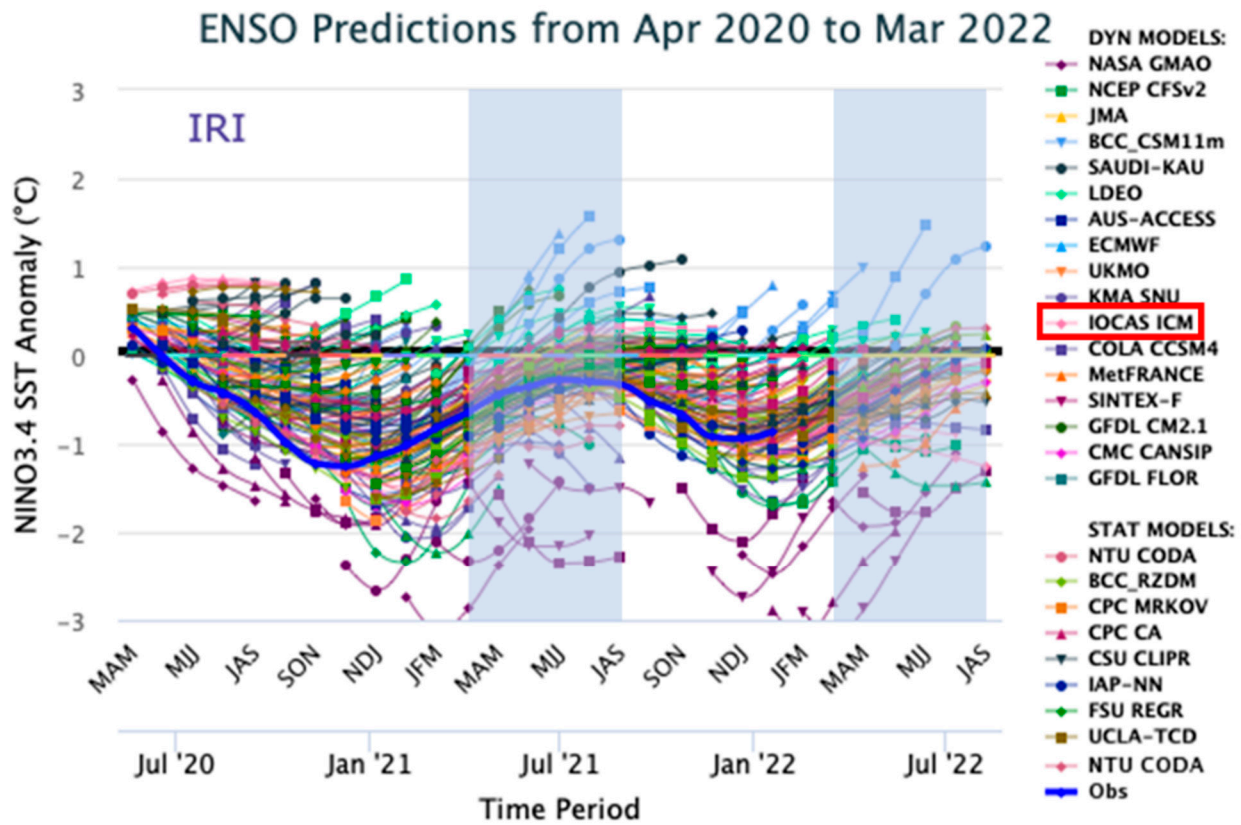


Figure 1. ENSO predictions provided by the IRI/CPC from April 2020 to March 2022.

IOCAS ICM (intermediate coupled model, developed at the Institute of Oceanology, Chinese Academy of Sciences) [9] stands out as one of the prediction models listed in Figure 1, which has provided ENSO forecasting for IRI/CPC since August 2015 and successfully predicted a strong El Niño event in 2015/2016 [10,11] and consecutive third La Niña events in 2020/2021, 2021/2022 and 2022/2023 [12,13]. Many researchers have utilized IOCAS ICM for ENSO predictability studies, including the maximal initial error [14,15], prediction barrier [14] and the sensitive area of target observation [16].

Reducing the initial field error is effective in improving the ENSO prediction skill [17,18], which inspires us to explore how the spatial structure of the error affects the prediction [19,20]. It is also critical to establish the characteristics of initial field errors in different seasons [21], which makes the error evolutions induce the SPB for ENSO prediction [22]. Further, identifying critical regions for intensive observation is also highly necessary to reduce the initial field error and minimize the forecast error [23–25]. The CNOP method [26] is used to study the optimal growth initial error (OGE) [27–29], which represents a perturbation under a given physical constraint, resulting in the largest nonlinear error evolution at the prediction time.

Previous studies explored the impact of optimal initial perturbation evolution of SSTA on ENSO forecasting using the ICM via the CNOP method. Mu et al. [30] determined the OPR (the optimal precursor) of SSTA in ENSO occurrence and explored the seasonal variation. Tao et al. [14] clarified the impact of the OGEs of SSTA and SLA across four seasons on the forecast results. All these studies obtained meaningful results, but the interaction

between SSTA and SLA cannot be ignored for ENSO from Bjerknes' theory [31,32]. Thermocline height anomalies (THA) expressed by sea level anomalies (SLA) reestablish vertical advection of the upper ocean and generate an upwelling pathway transported from the thermocline to the sea surface, thereby affecting the sea surface temperature (SST) [33,34]. Taking into account the joint effect of multivariable optimal initial errors is bound to reveal the distinctive mechanism of error growths and seasonal predictability barriers.

In this paper, we investigate the joint effects of SSTA and SLA for four seasons from the perspective of OGE. After determining the OGEs in four seasons of SSTA and SLA (i.e., SSTA-OGE, SLA-OGE and Joint-OGE), we first demonstrate the spatial structures and error growths of the OGEs for every season, respectively. Then, we perform the mechanism analyses on OGE evolutions. Finally, we conduct observing system simulation experiments to determine the effective economic observation network.

The rest of this paper is organized as follows: Section 2 describes the model and methods. Section 3 shows the experimental schema in detail. The main results, including the OGE patterns and evolutions, and related mechanism analyses are presented in Section 4, and the results of the observing system simulation experiments are presented in Section 5. Finally, the conclusion is given in Section 6. All abbreviations involved in this paper can be viewed in Table A1 in Appendix A.

2. Model and Methods

2.1. IOCAS ICM

The IOCAS ICM was developed by Zhang et al. [9] to simulate and predict ENSO events in the tropical Pacific, which consists of a dynamic ocean model and an empirical atmospheric model, as shown in Figure 2. The dynamic ocean model is based on IOM (intermediate ocean model, developed by Keenlyside and Kleeman [35]), an SST anomaly model and an T_e model (the temperature of subsurface water entrained into the mixed layer model). The empirical atmospheric model is a statistical model for wind stress (marked as τ model).

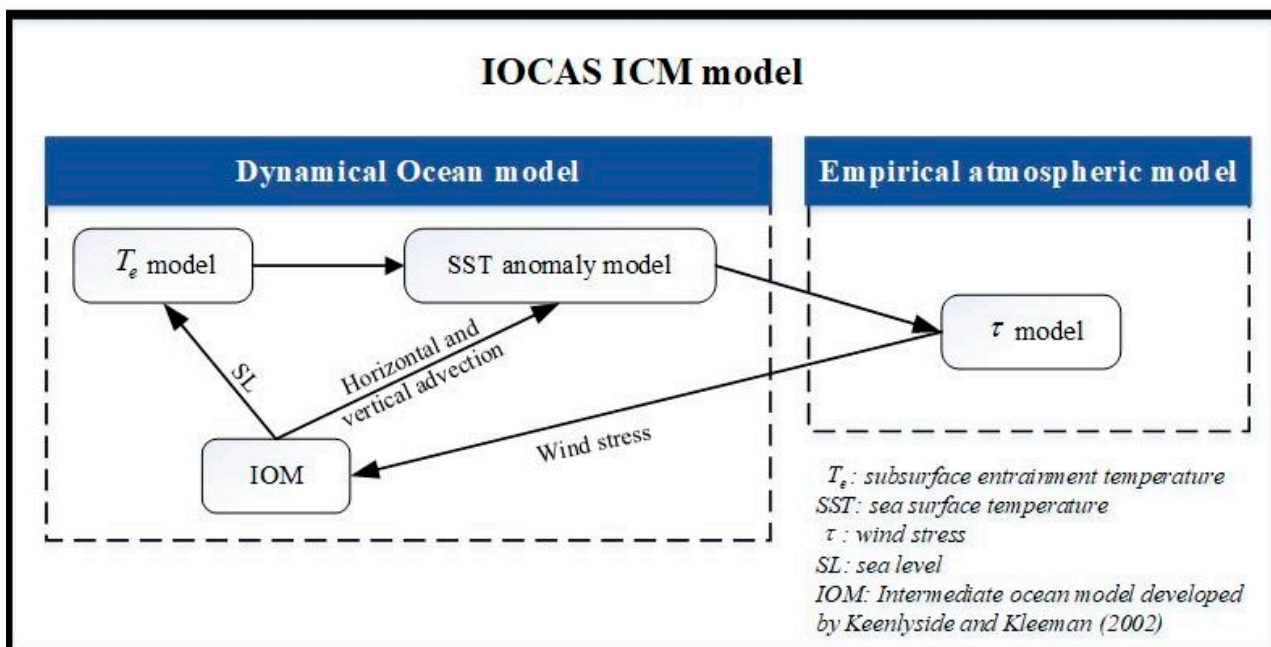


Figure 2. Component and the coupling relationship in IOCAS ICM [35].

By importing T_e , the ICM involves the interaction of sea–air physical variables between the surface layer and subsurface layer (e.g., sea surface current, sea vertical current, 20 °C depth anomalies, sea entrainment salinity, etc.), which improves the model simulation and prediction of sea surface temperature in the tropical Pacific. The ocean region of the ICM

extends from 31° S to 31° N and from 124° E to 30° E, which covers the tropical Pacific and Atlantic basins. The region for variables is divided into 134 × 61 grid points. In detail, it has 2° zonal grid spacing and a meridional grid stretching from 0.5° within 10° of the equator to 3° at the meridional northern and southern boundaries.

2.2. CNOP Method

The conditional nonlinear optimal perturbation (CNOP) method was proposed by Mu and Duan [26]. The following is a brief introduction to CNOP.

Assume that a meteorological numerical model can be simplified as follows:

$$\begin{cases} \frac{\partial \mathbf{U}}{\partial t} + F(\mathbf{U}) = 0, \\ \mathbf{U}|_{t=0} = \mathbf{U}_0, \end{cases} \tag{1}$$

where F is the nonlinear operator of the numerical model, $\mathbf{U}(t) = (\mathbf{U}_1(t), \mathbf{U}_2(t), \dots, \mathbf{U}_n(t))$ is the state at t time and \mathbf{U}_0 is the state at zero time (the initial state).

By adding initial perturbation \mathbf{u}_0 to the initial state, after the integration time T , we have

$$\mathbf{U}(T) + \mathbf{u}(T) = M(\mathbf{U}_0 + \mathbf{u}_0)(T) \tag{2}$$

where M is a propagator governed by the integration time and initial state, and $\mathbf{u}(T)$ describes the evolution of the initial perturbation \mathbf{u}_0 .

In general, \mathbf{u}_0 , which satisfies the initial perturbation constraint $\|\mathbf{u}_0\| \leq \delta$ and Equation (3), is represented as \mathbf{u}_0^* , i.e., the CNOP.

$$J(\mathbf{u}_0^*) = \max_{\|\mathbf{u}_0\| \leq \delta} \|M(\mathbf{U}_0 + \mathbf{u}_0)(T) - M(\mathbf{U}_0)(T)\|^2 \tag{3}$$

2.3. Solving CNOP of ICM with GD Algorithm

Solving CNOP of the numerical models is an optimization problem. Generally, the gradient of the numerical models when iterating every time step is calculated by the adjoint model. Mu et al. [36] adopted the gradient definition to obtain the gradient and successfully applied it to the ZC model. To effectively calculate the gradient of high-dimensional numerical models, firstly, the feature space (low-dimensional space) of numerical models is obtained, and then the gradient is calculated in the feature space through the gradient definition. Mu et al. [30,37] successfully applied it to MM5 and ICM models. In this paper, the same method is used to solve the CNOPs of ICM. Different from Mu et al. [30], there are three initial perturbations, whose nondimensionalized forms are $\overset{\rightarrow}{\mathbf{u}}_0^{\text{Joint}} = \begin{pmatrix} \overset{\rightarrow}{\mathbf{u}}_0^{\text{SLA}} & \overset{\rightarrow}{\mathbf{u}}_0^{\text{SSTA}} \end{pmatrix}$, $\overset{\rightarrow}{\mathbf{u}}_0^{\text{SLA}}$ and $\overset{\rightarrow}{\mathbf{u}}_0^{\text{SSTA}}$. They, respectively, represent simultaneously superimposing SLA and SSTA perturbations on the initial field, superimposing SLA perturbation and SSTA perturbation. Corresponding constraints are δ_{SLA} , δ_{SSTA} and δ_{Joint} as Equations (4)–(6). We integrate ICM for 200 years from 1960 to 2160; then, means and standard deviations of SSTA and SLA on grid point (i, j) are calculated.

$$\|\overset{\rightarrow}{\mathbf{u}}_0^{\text{SLA}}\| = \sqrt{\sum_{i,j} \left[\frac{\mathbf{u}_0^{\text{SLA}}(i,j) - \bar{\mathbf{U}}_{\text{SLA}}(i,j)}{\sigma_{\text{SLA}}(i,j)} \right]^2} \leq \delta_{\text{SLA}} \tag{4}$$

$$\|\overset{\rightarrow}{\mathbf{u}}_0^{\text{SSTA}}\| = \sqrt{\sum_{i,j} \left[\frac{\mathbf{u}_0^{\text{SSTA}}(i,j) - \bar{\mathbf{U}}_{\text{SSTA}}(i,j)}{\sigma_{\text{SSTA}}(i,j)} \right]^2} \leq \delta_{\text{SSTA}} \tag{5}$$

$$\|\overset{\rightarrow}{\mathbf{u}}_0^{\text{Joint}}\| = \sqrt{\sum_{i,j} \left[\frac{\mathbf{u}_0^{\text{SLA}}(i,j) - \bar{\mathbf{U}}_{\text{SLA}}(i,j)}{\sigma_{\text{SLA}}(i,j)} \right]^2 + \sum_{i,j} \left[\frac{\mathbf{u}_0^{\text{SSTA}}(i,j) - \bar{\mathbf{U}}_{\text{SSTA}}(i,j)}{\sigma_{\text{SSTA}}(i,j)} \right]^2} \leq \delta_{\text{Joint}} \tag{6}$$

On grid point (i, j) , $u_0^{SLA}(i, j)$ is the SLA perturbation, and $u_0^{SSTA}(i, j)$ is the SSTA perturbation. $\bar{U}_{SLA}(i, j)$ is the mean value of SLA, $\bar{U}_{SSTA}(i, j)$ is the mean value of SSTA. $\sigma_{SLA}(i, j)$ is the standard deviation of SLA and $\sigma_{SSTA}(i, j)$ is the standard deviation of SSTA.

The parameter settings for solving CNOP of ICM with the GD algorithm are in Table 1. The dimension of the feature space (DoF) is determined when the sum of corresponding eigenvalues reaches 95% of the whole feature space [30]. After multiple experiments, the proper δ is ascertained to avoid too-large constraint leading to the forecast results deviating from natural laws or too-small constraint causing unobvious error evolution. In our experiment, δ_{SLA} and δ_{SSTA} are set to 15, and δ_{joint} is set to 20. The maximum iteration step (Maxit) is set to 50, which can ensure the convergence and efficiency of SPG2. The integrating time of ICM (lead time) is set to 12 months for ENSO, generally going through 12 months from the growth phase to the mature phase [28].

Table 1. The parameter settings for solving CNOP of ICM with the GD algorithm.

Parameters	Value			Meaning
	SSTA	SLA	Joint	
DoF	48	48	72	Dimension of the feature space
δ	15	15	20	The constraint of the initial perturbation
Maxit	50			The maximum iteration step of SPG2
Lead time (T)	12 months			The integrating time of ICM

3. Experimental Schema

We integrate the ICM model from 1960 to 2000 (Figure 3a) and then select two reference states, namely the El Niño event in 1982/1983 (Figure 3b) and the La Niña event in 1984/1985 (Figure 3c). For each reference state, we mark the year when it reaches mature phase as year (1). The year prior to year (1) is marked as year (0), and the year preceding year (0) is referred to as year (−1). We focus on the onset phases of the reference states (from July (−1) to June (0)).

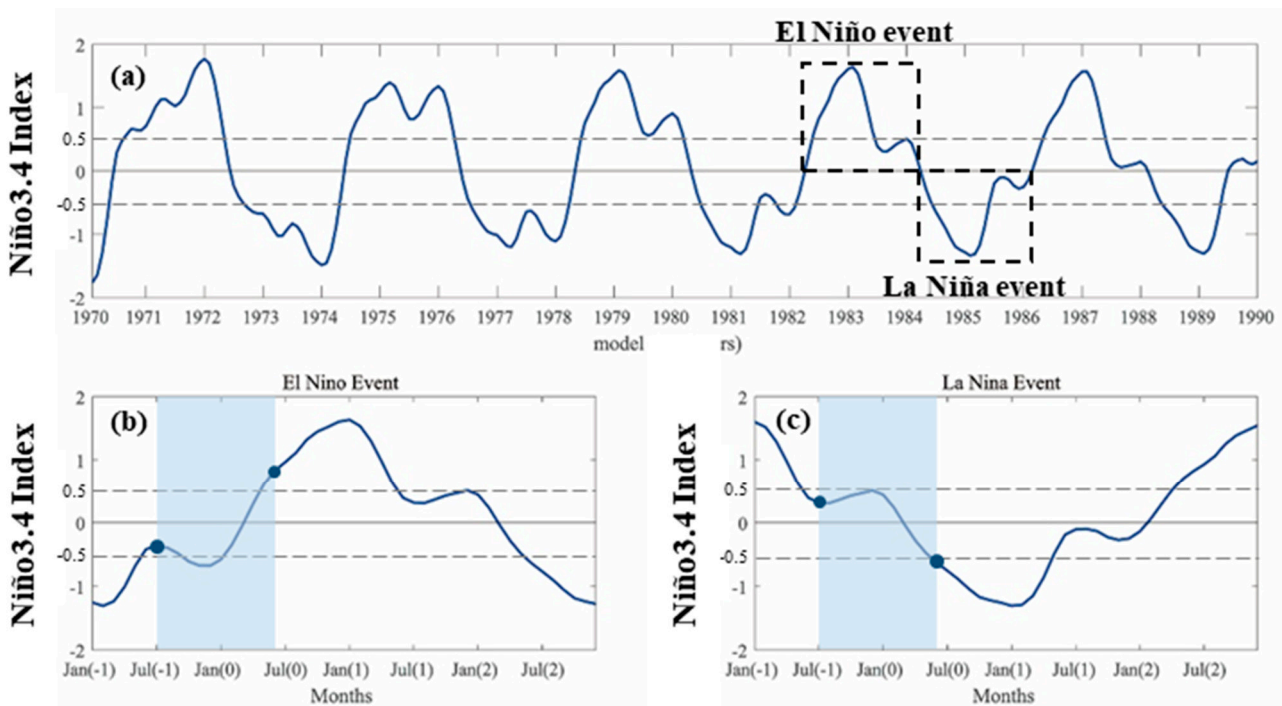


Figure 3. (a) Niño3.4 index (°C) when integrating the ICM model from 1960 to 2000. (b) Selected reference states for the El Niño event. (c) Selected reference states for the La Niña event. The blue rectangles from July (−1) to June (0) are the onset phase of events.

For the El Niño reference state, we take each month from July (−1) to June (0) as the start month and integrate the ICM model for 12 months to obtain the simulation results. Then, we, respectively, superimpose the SSTA, SLA and joint perturbation on the initial field and integrate them to obtain the simulation results, i.e., $M(\mathbf{U}_0 + \mathbf{u}_0)(T)$ in Equation (2). According to Equation (3) in Section 2.2, we solve CNOPs of ICM with GD algorithm to obtain 36 CNOPs for the El Niño reference state. Similarly, we also obtain 36 CNOPs for the La Niña reference states. Remarkably, we discovered that the 36 CNOPs for the El Niño reference state are the same as those for the La Niña reference state. Moreover, when we select other El Niño or La Niña events from Figure 3a as reference states, we also obtain the same 36 CNOPs. In other words, the resulting CNOPs are found to be independent of the reference state.

The obtained CNOPs (i.e., \mathbf{u}_0^* in Equation (3)) stand for optimally growing initial errors (OGEs). We accordingly mark them as SSTA-OGEs for the SSTA perturbation, SLA-OGEs for the SLA perturbation and Joint-OGEs for the joint perturbation. Notably, there are a total of 12 OGEs for each type of perturbation, with each OGE corresponding to the start month from July (−1) to June (0).

To analyze the seasonal dependence of OGEs for each type of perturbation, we obtain summer OGEs, autumn OGEs, winter OGEs and spring OGEs by averaging OGEs of three months (July (−1), August (−1), September (−1)), (October (−1), November (−1), December (−1)), (January (0), February (0), March (0)) and (April (0), May (0), June (0)), respectively. That is, there are 4 seasonal OGEs for each type of perturbation.

For each selected reference state, we evaluate the error evolutions of seasonal OGEs by comparing the simulation results of integrating the ICM model for 12 months, with or without superimposing summer OGEs, autumn OGEs, winter OGEs and spring OGEs on the initial field, respectively (August (−1), October (−1), February (0) and May (0) as the start month). For investigating the error evolutions of seasonal OGEs over 12 months, we also integrate ICM for 3, 6 and 9 months, in addition to 12 months. To demonstrate the SPB resulting from seasonal OGE, we obtain the total error evolution every month by calculating the root square mean for the error evolution of each grid over 12 months. The growth rate is also used to measure the SPB. The experiment results are shown in Section 4.1.

The mechanism analysis on error evolutions of SLA-OGE, SSTA-OGE and Joint-OGE is performed in Section 4.2. Then, we show the observing system simulation experiment results in Section 5.

4. Result Analyses

4.1. Patterns, Evolutions of OGEs and the Resulting SPB

4.1.1. SLA-OGEs

Figure 4 shows the patterns of seasonal SLA-OGEs and the simulation results after integrating ICM for 12 months, with and without superimposed SLA-OGEs on the initial field of El Niño/La Niña reference state.

From Figure 4(1), the patterns of four seasonal SLA-OGE show dipole distribution, with the negative in the west and the positive in the east. In other words, SLA-OGEs exhibit almost no seasonal dependence. For the El Niño reference state, whether SLA-OGEs are superimposed or not, all events reach the mature phase, and the simulation results for each season are the same as Figure 4(2),(3). For the La Niña reference state, the same phenomenon also occurs in Figure 4(4),(5). It indicates that SLA-OGEs do not trigger error evolution.

Figure 5 displays the total error evolution and its growth rate every month for four seasonal SLA-OGEs over 12 months for two selected reference states. It can be seen that the total error evolutions are all less than 0.25, which indicates that seasonal SLA-OGEs have almost no impact on ENSO evolutions. Likewise, despite the growth rates showing regular fluctuations for seasonal SLA-OGEs, they are too little in magnitude to be considered as a predictability barrier.

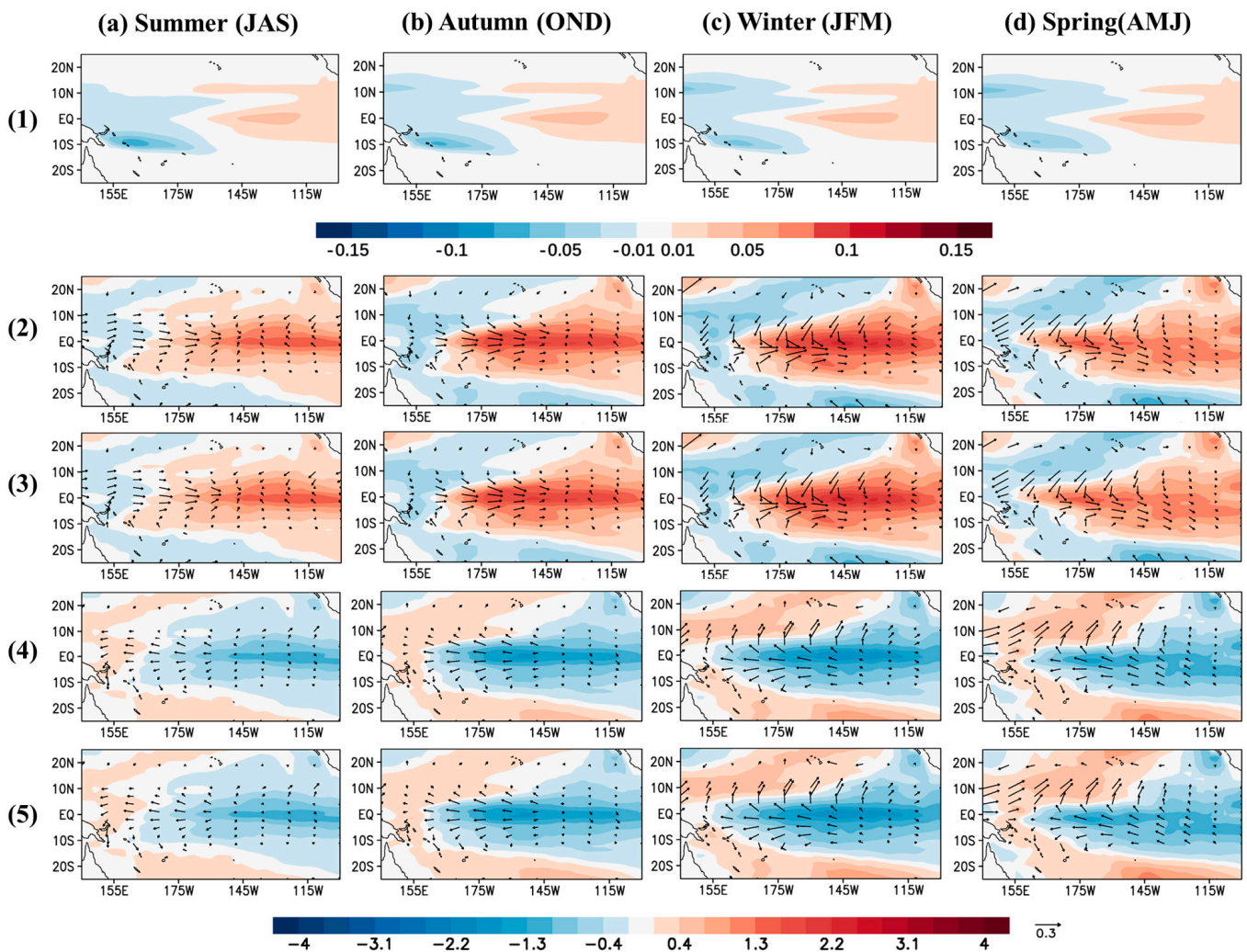


Figure 4. The patterns of seasonal SLA–OGEs and the simulation results after integrating ICM for 12 months, with and without superimposing SLA–OGEs on the initial field of El Niño/La Niña reference state. (1) SLA–OGE patterns; (2) the simulation results for SSTA (°C) and wind stress anomalies (dyn/cm²) without superimposing SLA–OGEs on the initial field of El Niño reference state; (3) the same as (2), superimposing SLA–OGEs; (4) the same as (2) for La Niña reference state; (5) the same as (4), with superimposing SLA–OGEs.

4.1.2. SSTA-OGEs

Figure 6 shows the patterns of seasonal SSTA-OGEs and the simulation results after integrating ICM for 12 months, with and without superimposed SSTA-OGEs on the initial field of El Niño/La Niña reference state. From Figure 6(1), the patterns of spring and summer SSTA-OGEs exhibit positive SSTA in the central and eastern Pacific Ocean, which almost covers the Niño3 and Niño4 areas. Those of autumn and winter SSTA-OGEs keep a kind of seesaw-like structure, with a negative SSTA in the west and a positive SSTA in the east. That is, SSTA-OGEs possess obvious seasonal dependence.

From Figure 6(2),(3), SSTA with superimposed summer and spring SSTA-OGEs on the initial field has more intense amplitudes and SSTA with superimposed autumn, and winter SSTA-OGEs have weaker amplitudes for the El Niño reference state. For the La Niña reference state, the opposite situation occurs from Figure 6(4),(5). It indicates that seasonal SSTA-OGEs have different effects on the evolution of El Niño or La Niña events.

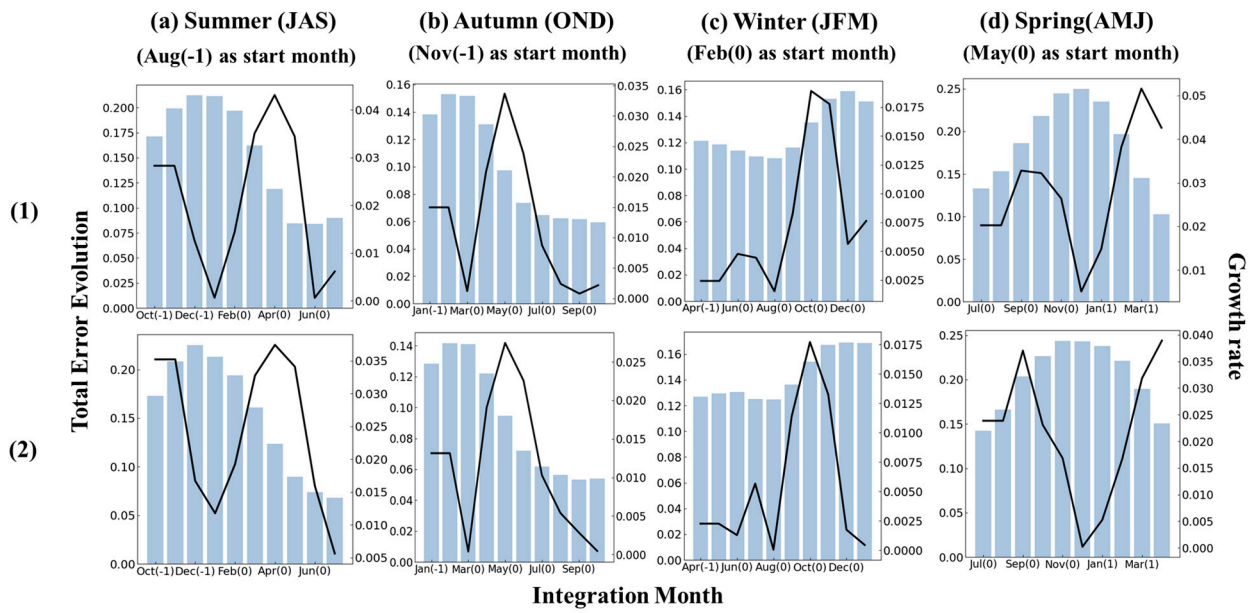


Figure 5. The total error evolution (histogram, left axis) and its growth rate (curves, right axis) every month for four seasonal SLA–OGEs over 12 months. The first two months are omitted considering the unstable initial phase. (1) For El Niño reference state, (2) for La Niña reference state.

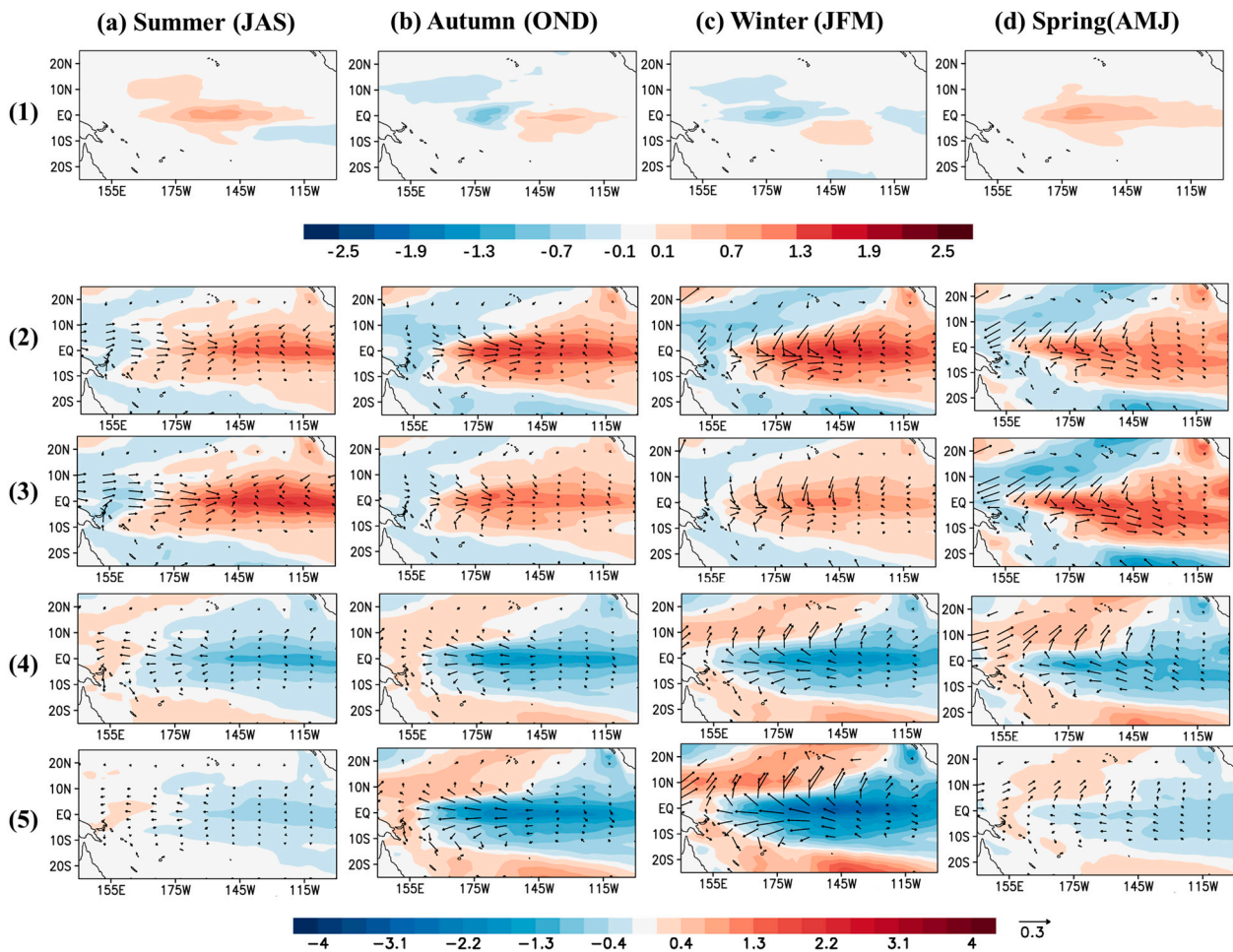


Figure 6. The patterns of seasonal SSTA–OGEs and the simulation results after integrating ICM for 12 months, with and without superimposing SSTA–OGEs on the initial field of the El Niño/La Niña

reference state. (1) SSTA patterns of SSTA–OGE; (2) the simulation results for SSTA ($^{\circ}\text{C}$) and wind stress anomalies (dyn/cm^2) without superimposing SSTA–OGEs of El Niño reference state; (3) the same as (2), with superimposing SSTA–OGEs; (4) the same as (2), for La Niña reference state; (5) the same as (4), with superimposing SSTA–OGEs.

To further investigate the evolutions of seasonal SSTA–OGEs, the patterns and the evolutions of four seasonal SSTA–OGEs in 3, 6, 9 and 12 months are shown in Figure 7. The evolution of summer SSTA–OGE in Figure 7a is characterized by the warming anomalies growth, which is rapid in the western tropical Pacific, spreading eastward and dispersing the cooling anomalies in the eastern Pacific. With the enhancement of westerly wind anomalies, the warming anomalies are further propelled and amplified in the eastern Pacific.

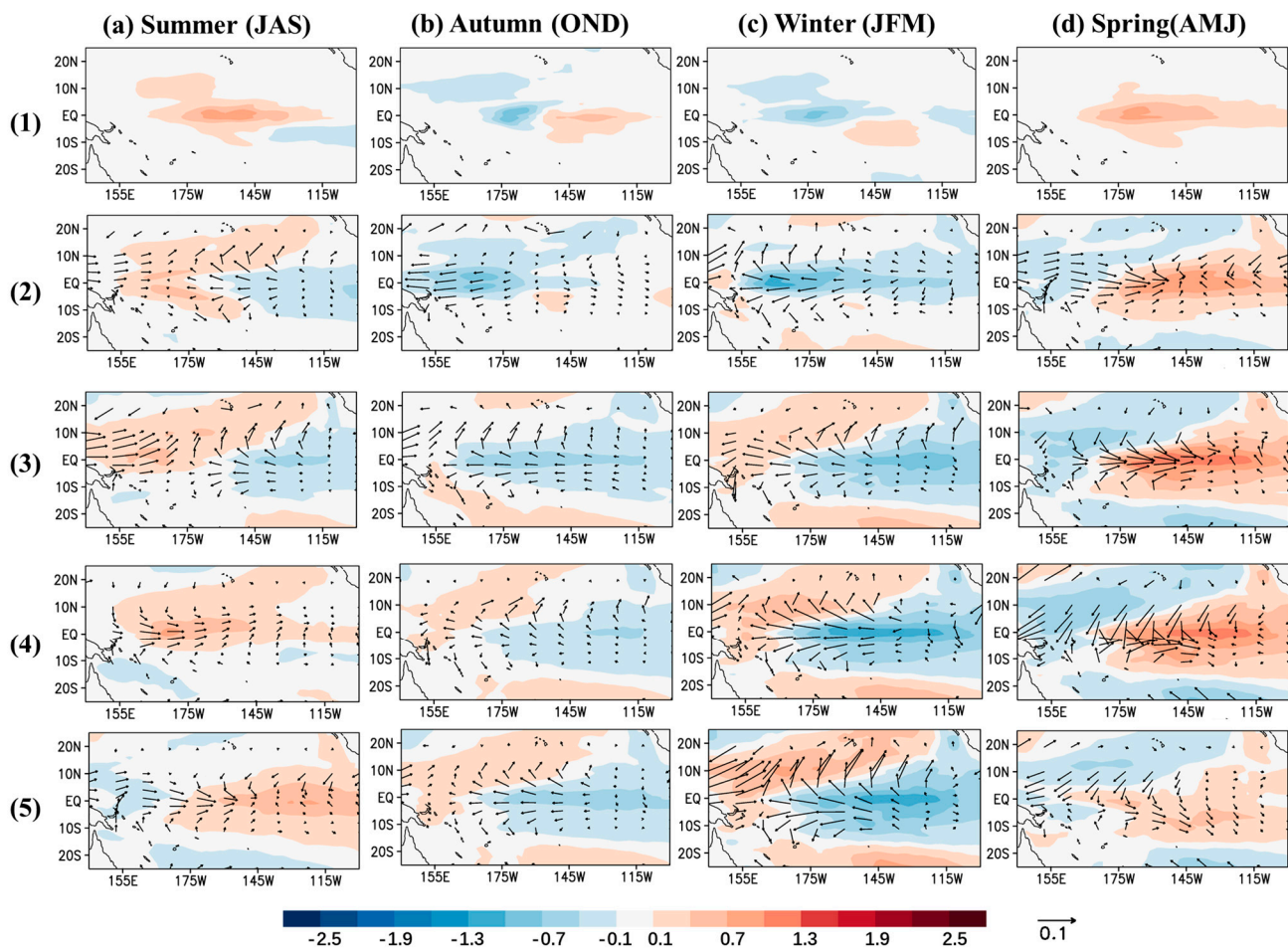


Figure 7. The patterns and the evolutions of seasonal SSTA–OGE over 12 months. (1) SSTA–OGE patterns; (2) evolution of SSTA–OGE for SSTA ($^{\circ}\text{C}$) and wind stress anomalies (dyn/cm^2) in summer (a), autumn (b), winter (c) and spring (d) for 3 months; (3) the same as (2), for 6 months; (4) the same as (2), for 9 months; (5) the same as (2), for 12 months.

From Figure 7b, the evolution of autumn SSTA–OGE depicts that the cooling anomalies first appear in the western-central Pacific and then extend eastward. Along with the easterly wind stress anomalies, the cooling anomalies converge in the eastern Pacific, while warming anomalies gradually intensify in the western Pacific. In addition, from Figure 7c, the evolution of winter SSTA–OGE is almost consistent with autumn SSTA–OGE. From Figure 7d, the evolution of spring SSTA–OGE shows large positive SSTA accumulated in the eastern equatorial Pacific, while negative SSTA converges in the western Pacific. Then,

the westerly anomalies carry the negative SSTA eastward and weaken the positive SSTA in the equatorial eastern Pacific.

In brief, the summer and spring SSTA-OGEs propel SSTA in the central-eastern tropical Pacific to grow toward the positive phases, leading to overestimating El Niño events and underestimating La Niña events. The evolution difference is that the evolution of summer SSTA-OGE undergoes a transition from the negative to positive phase, while the evolution of spring SSTA-OGE undergoes a transition from maturity to decay in the positive phase. On the contrary, the autumn and winter SSTA-OGEs propel SSTA in the central-eastern tropical Pacific to grow toward the negative phases, which leads to underestimating El Niño events and overestimating La Niña events. The evolutions of autumn and winter SSTA-OGEs are similar, differing only in terms of stronger magnitude for winter.

Figure 8 illustrates the total error evolution and its growth rate every month for four seasonal SSTA-OGEs over 12 months for two selected reference states. The total error evolutions are all large for four seasonal SSTA-OGEs, indicating that SSTA-OGEs have a significant seasonal impact on ENSO evolutions.

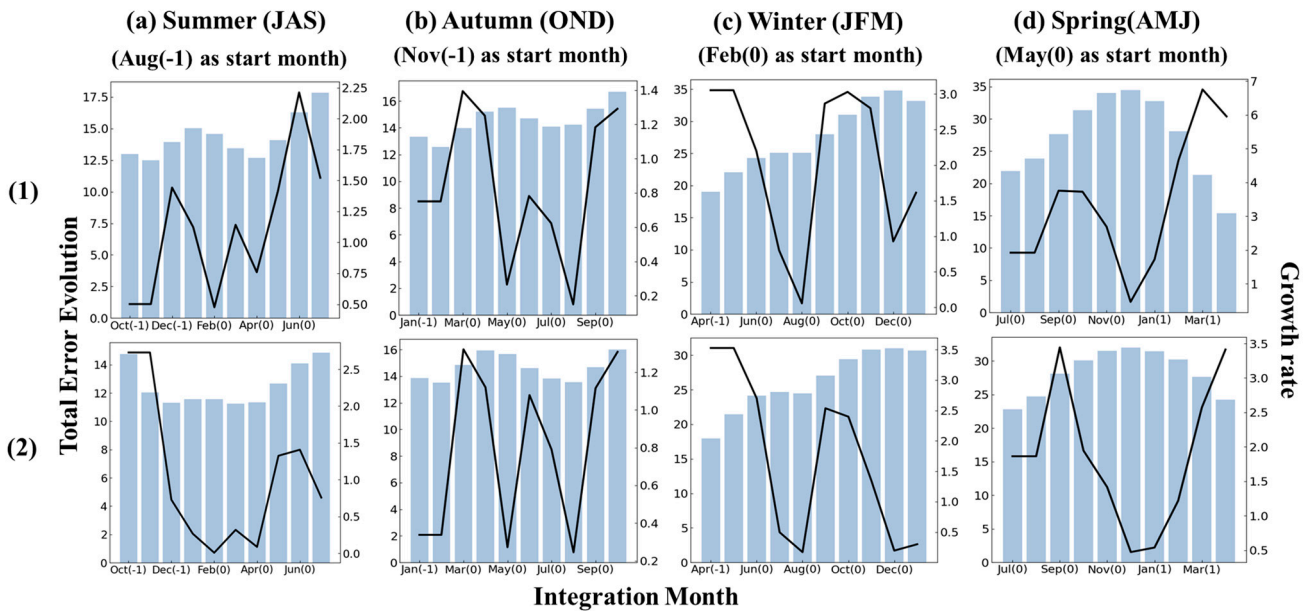


Figure 8. The total error evolution (histogram, left axis) and its growth rate (curves, right axis) every month for four seasonal SSTA–OGEs over 12 months. The first two months are omitted considering the unstable initial phase. (1) For El Niño reference state, (2) for La Niña reference state.

For the El Niño reference in Figure 8(1), the SPB occurs in mid to late spring of the next year for summer SSTA-OGE, in early spring of the next year for autumn and spring SSTA-OGEs and in the entire spring of the next year for winter SSTA-OGE. For La Niña reference state in Figure 8(2), the SPB occurs in the same phase, although the largest growth rate is in October (–1) for autumn SSTA-OGE, which is only in the unstable phase of ICM. There are varying intensities of SPB caused by seasonal SSTA-OGEs, with the strongest resulting from spring SSTA-OGE, followed by winter and summer SSTA-OGEs, and the weakest is autumn.

4.1.3. Joint-OGEs

Figure 9 shows the patterns of seasonal Joint-OGEs and the simulation results after integrating ICM for 12 months, with and without superimposing Joint-OGEs on the initial field of the El Niño/La Niña reference state. For Figure 9(1), the patterns of summer, spring and winter Joint-OGEs in SLA exhibit dipole distribution, with negative anomalies in the west and positive anomalies in the east. However, for autumn Joint-OGE, the positive SLA is distributed along the equatorial Pacific, and the negative SLA is located on both

sides. From Figure 9(2), the patterns of spring and summer Joint-OGEs in SSTA emerge as positive anomalies in the central-eastern Pacific Ocean and show positive anomalies near the dateline in the central Pacific for autumn and winter Joint-OGEs. In total, Joint-OGEs are relatively less sensitive to the season than SSTA-OGEs. Furthermore, Joint-OGEs are not the results of SSTA-OGEs plus SLA-OGEs linearly, which indicates that Joint-OGEs contain nonlinear characteristics between multivariable optimal initial perturbation.

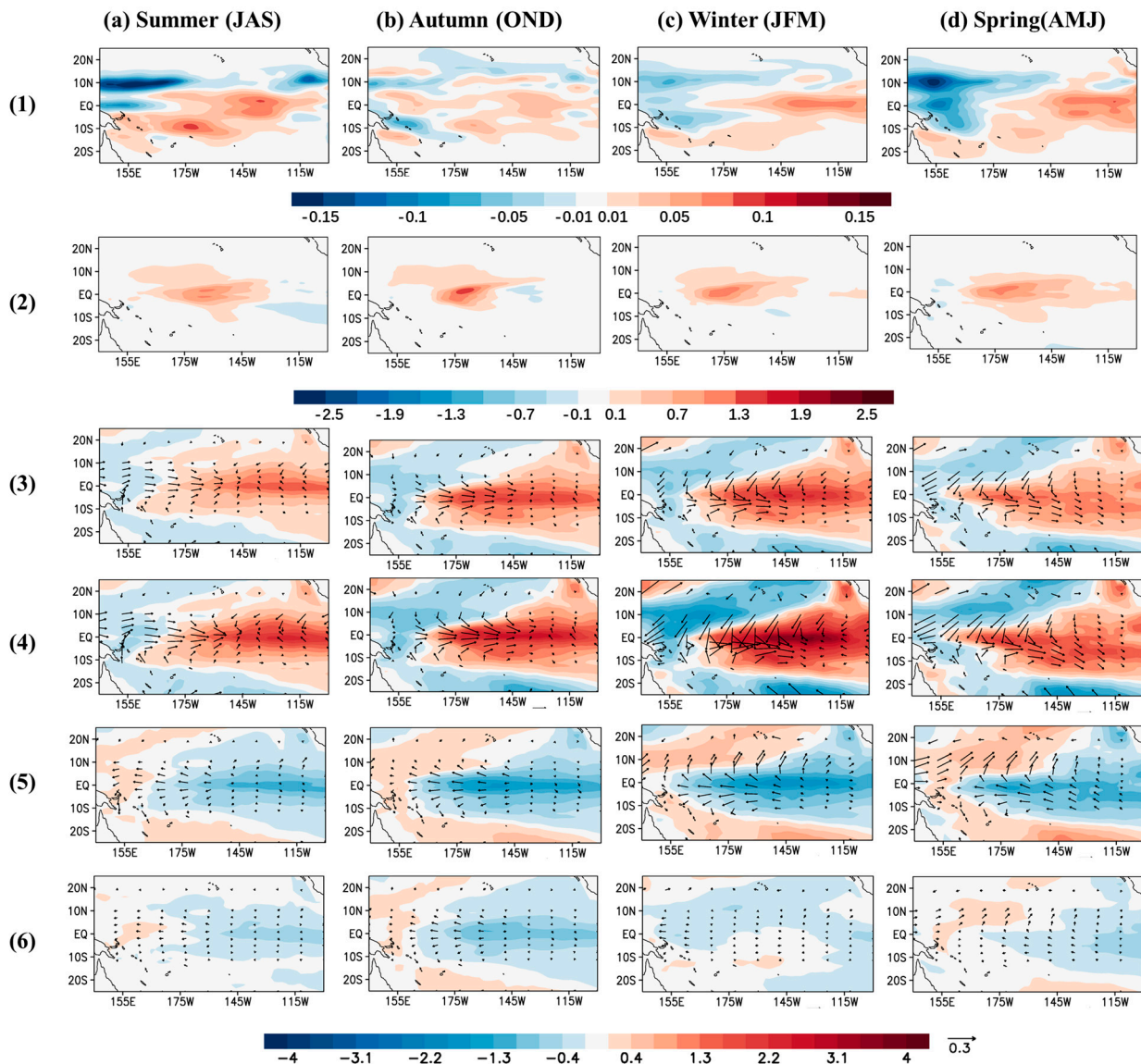


Figure 9. The patterns of seasonal Joint-OGEs and the simulation results after integrating ICM for 12 months, with and without superimposing Joint-OGEs on the initial field of the El Niño/La Niña reference state. (1) SLA patterns of Joint-OGE; (2) SSTA patterns of Joint-OGE; (3) the simulation results for SSTA ($^{\circ}\text{C}$) and wind stress anomalies (dyn/cm^2) without superimposing Joint-OGEs on the initial field of El Niño reference state; (4) the same as (3), with superimposing Joint-OGEs; (5) the same as (4), for La Niña reference state; (6) the same as (5), with superimposing Joint-OGEs.

From Figure 9(3),(4), SSTA with superimposed all-seasonal Joint-OGEs on the initial field has more intense amplitudes for the El Niño reference state. For the La Niña reference state, the opposite situation occurs from that in Figure 9(5),(6). These results demonstrate that Joint-OGEs also greatly impact the evolution of El Niño or La Niña events.

Figure 10 describes the patterns and the evolutions of seasonal Joint-OGEs in 3, 6, 9 and 12 months. For the evolution of summer Joint-OGE in Figure 10a, both the positive SSTA

and the westerly wind anomalies first appear in the western Pacific and then propagate to the eastern Pacific. As the integration time increases, the warming anomalies occupy the eastern Pacific and are further enhanced.

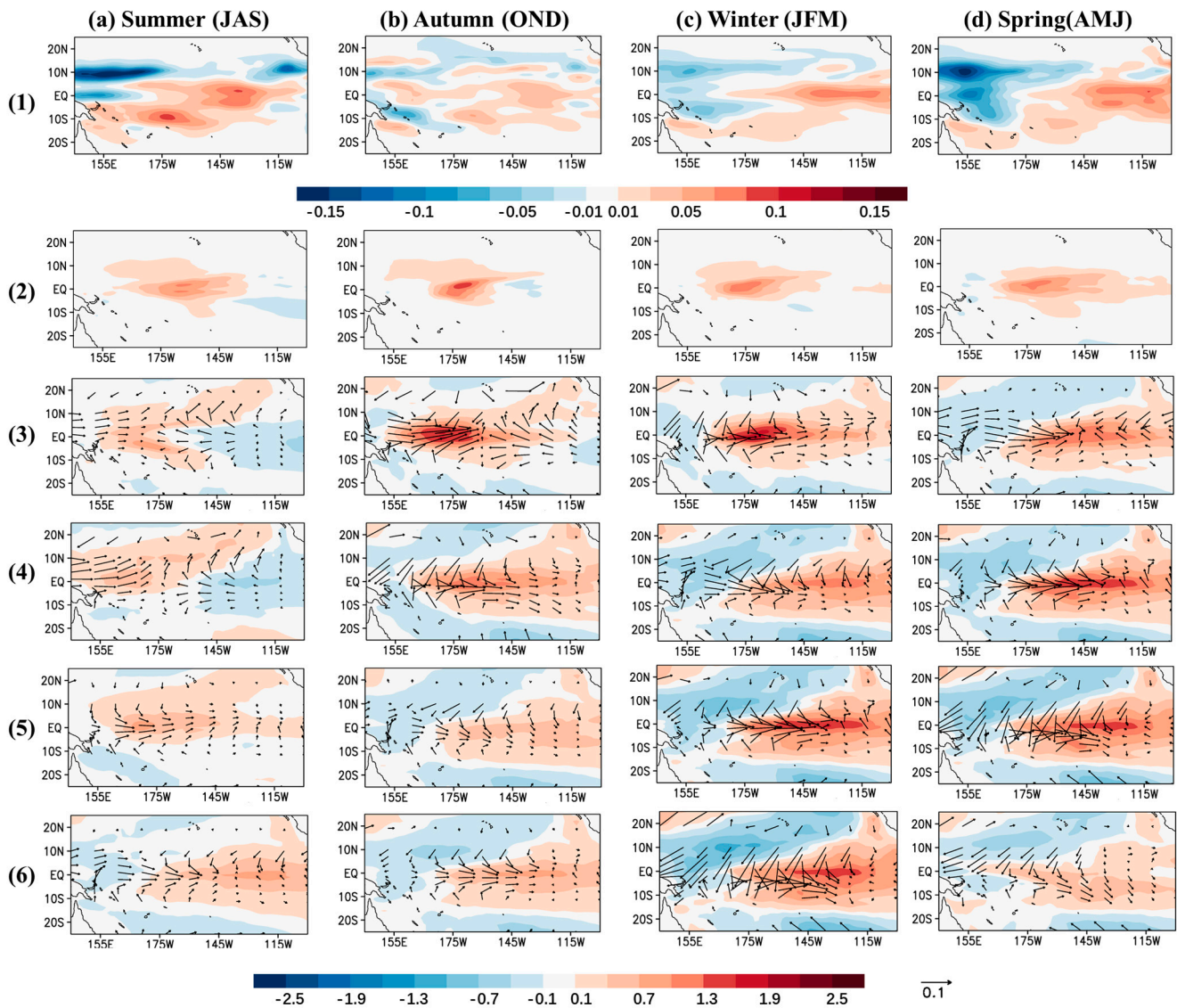


Figure 10. The patterns and the error evolutions of seasonal Joint–OGE over 12 months. (1) The SLA pattern of Joint–OGE; (2) the SSTA pattern of Joint–OGE; (3) error evolution of Joint–OGE for SSTA ($^{\circ}\text{C}$) and wind stress anomalies (dyn/cm^2) in summer (a), autumn (b), winter (c) and spring (d) for 3 months; (4) the same as (3), for 6 months; (5) the same as (3), for 9 months; (6) the same as (3), for 12 months.

For the evolution of autumn Joint-OGE in Figure 10b, at the early stage, the continuous warmth is induced by positive SSTA and westerly wind anomalies over the central-eastern tropical Pacific. Then, along with an accumulation of cooling anomalies in the western tropical Pacific, the warming anomalies in the eastern Pacific continually amplify. Likewise, from Figure 10c, the evolutions of winter Joint-OGE are almost consistent with autumn Joint-OGE.

From Figure 10d, the evolution of spring Joint-OGE manifests that along with the easterly anomalies, warming anomalies continue to amplify in the eastern Pacific. Then, the positive SSTA in the eastern Pacific is gradually erased by negative SSTA from the western Pacific.

In summary, when the initial field contains the Joint-OGE type of perturbation, with enhanced ocean–atmosphere interactions, error growths are more pronounced than SSTA-OGE and SLA-OGE. All seasonal Joint-OGEs propel SSTA in the central-eastern tropical Pacific to grow toward the positive phases, leading to overestimating the El Niño events and underestimating the La Niña events. The evolution difference is that the summer Joint-OGE undergoes a transition from negative to positive. The autumn and winter Joint-OGE is from the onset to maturity of the positive phase; only the winter OGE has stronger magnitude. Meanwhile, the spring OGE undergoes a transition from maturity to decay of the positive phase.

Figure 11 illustrates the total error evolution and its growth rate every month for four seasonal Joint-OGEs over 12 months for two selected reference states. All seasonal Joint-OGEs have larger total error evolutions than SSTA-OGEs and SLA-OGEs, which indicates that Joint-OGEs also have a significant influence on ENSO evolutions, with evident seasonal effects.

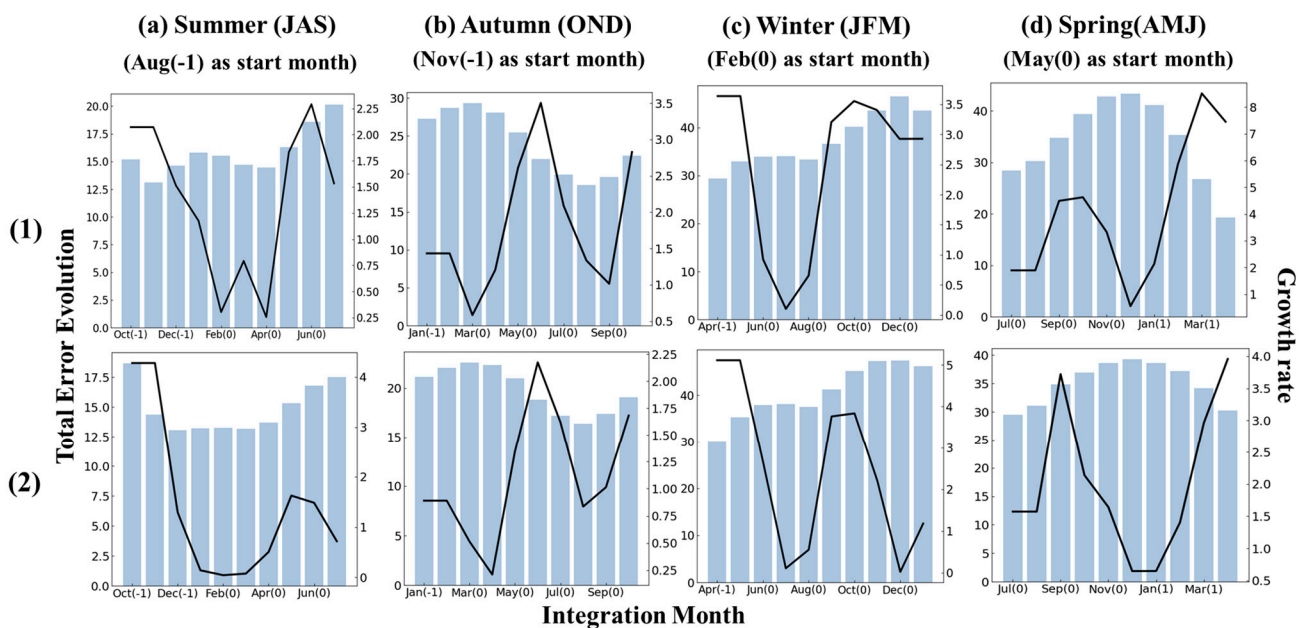


Figure 11. The total error evolution (histogram, left axis) and its growth rate (curves, right axis) of every month for four seasonal Joint–OGEs over 12 months. The first two months are omitted considering the unstable initial phase. (1) for El Niño reference state, (2) for La Niña reference state.

The results of growth rates manifest that all seasonal Joint-OGEs induce the SPB with more significant intensity than SSTA-OGEs and SLA-OGEs. For the El Niño reference state in Figure 11(1), the SPB occurs in mid to late spring of the next year for summer Joint-OGE, in the entire spring to early summer for autumn Joint-OGE, in the entire spring of the next year for winter Joint-OGE and in early spring of the next year for spring Joint-OGEs. Additionally, the SPB occurs in the same phase for La Niña reference state in Figure 11(2) and, as with the autumn SSTA-OGE, the autumn Joint-OGE presents the same exception for the same reason. Moreover, the most intense SPB is caused by the spring Joint-OGE, followed by winter, and the weaker is autumn and summer.

4.2. The Mechanism Analysis on OGE Evolutions and SPB

Mechanism analyses on OGE evolutions and SPB are performed in this section. We illustrate the evolutions of OGEs in several crucial variates (Z_{20} , SLA, etc.) to provide an exhaustive demonstration of the error evolution dynamics and the SPB process.

4.2.1. Dynamics Analysis on SLA-OGEs

From the conclusions in Section 4.1.1, all seasonal SLA-OGEs have almost no impact on event evolutions with total error evolutions less than 0.25. This is explainable through the Bjerknes positive feedback [31]. The SSTA and THA are essential factors that induce ocean state changes. Despite SLA-OGEs impacting oceanic thermocline to some extent, the stable SSTA counteracts the feeble effects of THA, eliminating the ENSO deviation after a few weeks of integration.

4.2.2. Dynamics Analysis on SSTA-OGEs

From the conclusions in Section 4.1.2, all seasonal SSTA-OGEs significantly impact the evolution of ENSO events and induce SPB. By taking winter as an example, we derive an explicit and full-cycle understanding of the error evolution dynamics and SPB origin for SSTA-OGEs (the mechanisms for other seasonal SSTA-OGEs are consistent with winter).

Figure 12 displays the evolution of the winter SSTA-OGE in SSTA and wind stress anomalies, T_e , SLA and 20 °C depth anomalies (Z_{20}) for 3, 6, 9 and 12 months. From Figure 12(1),(2), in the early stage, the cooling anomalies first concentrate in the central Pacific and propagate eastward accompanied by easterly anomalies. During this time, the eastward Kelvin wave and westward Rossby wave are triggered. Due to an upwelling Kelvin wave and easterly anomalies, shallow thermocline promotes the cooling effects of the sea subsurface in the eastern tropical Pacific, which continuously penetrate the surface. The Bjerknes positive feedback is generated in the tropical Pacific, which leads to rapid error growth and the SPB in the early integration period. From Figure 12(3),(4), at the later stage of integration, the Rossby wave turns back at the western boundary of the Pacific, which carries the warming anomalies, dispersing the cold anomalies in the central-eastern Pacific and attenuating Bjerknes positive feedback.

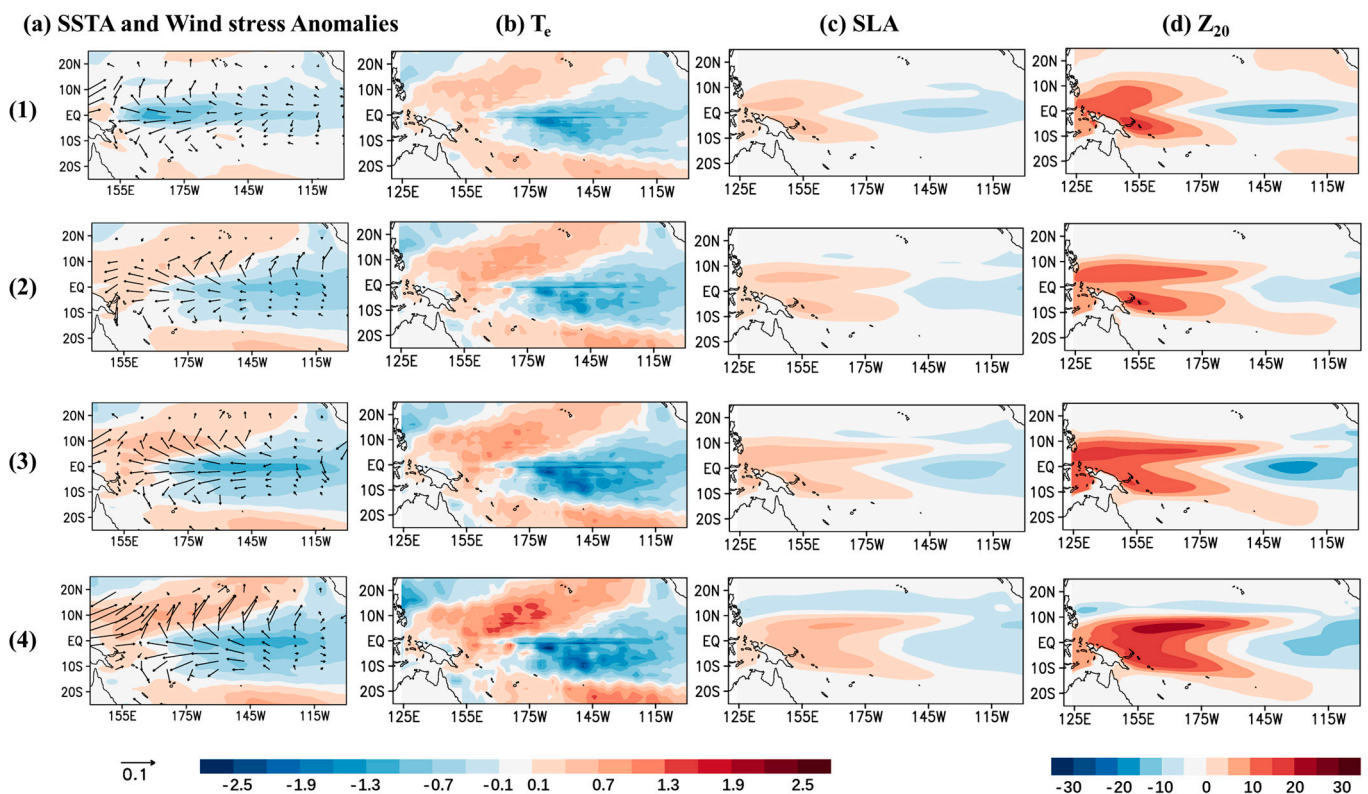


Figure 12. Evolutions of winter SSTA–OGE over 12 months. (1) Error evolution for (a) SSTA (°C) and wind stress anomalies (dyn/cm²), (b) T_e (°C), (c) SLA (m) and (d) Z_{20} for 3 months; (2) the same as (1), for 6 months; (3) the same as (1), for 9 months; (4) the same as (1), for 12 months. The contour interval is 5 m for Z_{20} .

To summarize, the evolutions of SSTA-OGEs are consistent with the ENSO dynamic. In addition, the principal physical processes involved in SSTA-OGE evolutions also govern the SPB, whose dynamics primarily involve establishing and attenuating Bjerknes positive feedback.

4.2.3. Dynamics Analysis on Joint-OGEs

From the conclusions in Section 4.1.3, all seasonal Joint-OGEs result in error growths and SPB with more significant intensity than SSTA-OGEs and SLA-OGEs. For dynamic analysis, the evolution of winter Joint-OGE in SSTA and wind stress anomalies, T_e , SLA and Z_{20} for 3, 6, 9 and 12 months is exhibited in Figure 13. From Figure 13(1),(2), large-scale warming anomalies concentrate in the central tropical Pacific and then propagate eastward, with strengthened westerly wind anomalies. Downwelling Kelvin waves characterized by the deepened thermocline are triggered and propagate eastward. Meanwhile, the dipole SLA pattern of Joint-OGE promotes coherent warming at the subsurface, and the Bjerknes feedback is set up to enlarge the error growth. Through thermal transmission and convection, the warming anomalies at the subsurface then penetrate the surface, further enhancing the warming effect in the eastern tropical Pacific and causing the SPB.

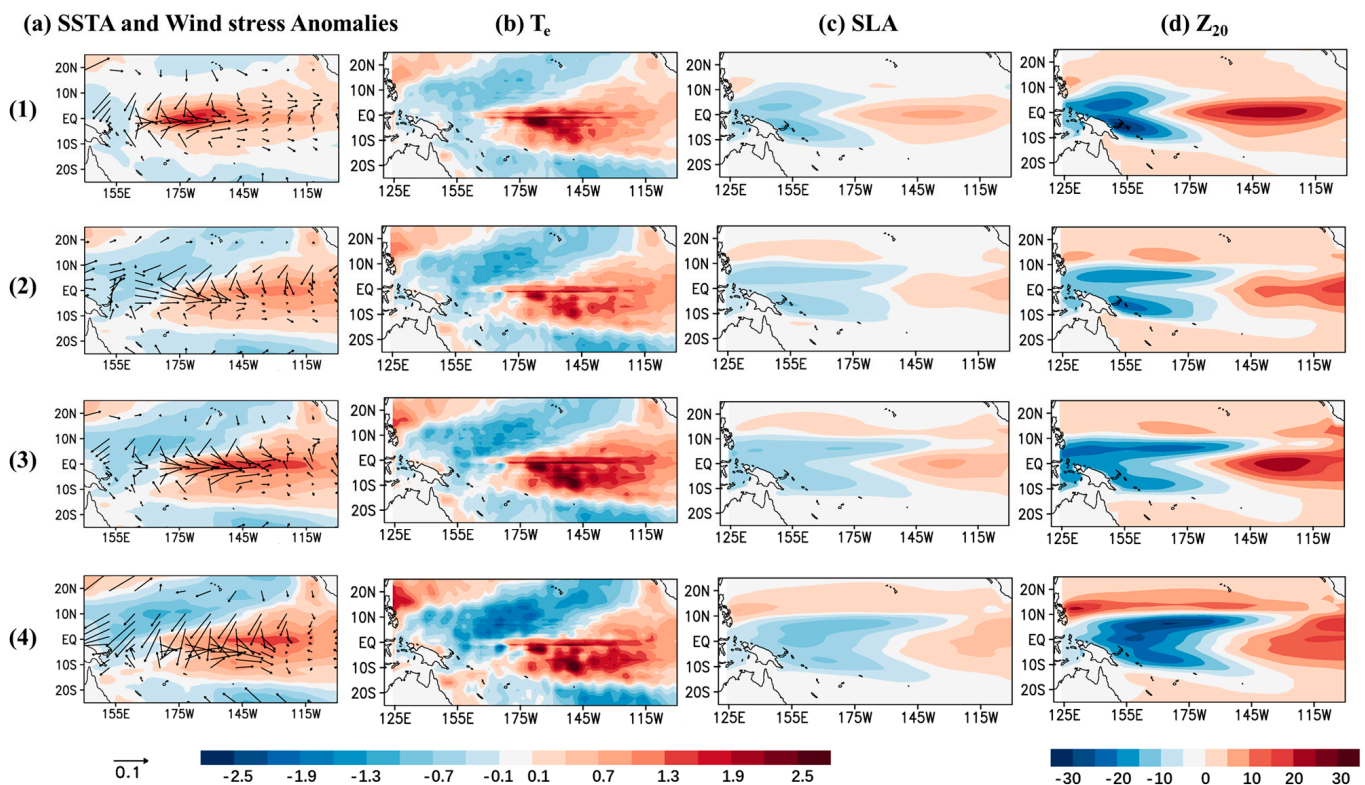


Figure 13. Evolutions of winter Joint-OGE over 12 months. (1) Error evolution for (a) SSTA ($^{\circ}\text{C}$) and wind stress anomalies (dyn/cm^2), (b) T_e ($^{\circ}\text{C}$), (c) SLA (m) and (d) Z_{20} for 3 months; (2) the same as (1), for 6 months; (3) the same as (1), for 9 months; (4) the same as (1), for 12 months. The contour interval is 5m for Z_{20} .

From Figure 13(3),(4), as the integration time increases, the apparent dispersion of the $20\text{ }^{\circ}\text{C}$ isotherm within the tropical Pacific is observed, which indicates that there is continuous thermal diffusion toward the mid-latitudes. At the same time, the upwelling Rossby wave propagates westward beyond the equator and reaches the western boundary. With the Rossby wave back, a large SLA appears in the western boundary and transmits eastward along the equator. Subsequently, the positive SSTA in the eastern Pacific Ocean is dispersed by the negative SSTA from the western tropical Pacific, which increases the forecasting uncertainty.

Briefly, the evolutions of seasonal Joint-OGEs are characterized by an El Niño-like evolution. The main physical processes involved in Joint-OGE evolutions also dominate the SPB, whose dynamics primarily contain the continuous heating between the upper ocean combined with Bjerknes feedback and the thermal diffusion in response to the discharge process.

In particular, the SPB induced by autumn SSTA-OGE and Joint-OGE presents a significant distinction, which manifests that the autumn SSTA-OGE produces the SPB occurring in early spring, but the autumn Joint-OGE persists for the entirety of spring to early summer. This is due to the dominance of the positive SSTA and SLA in autumn Joint-OGE (the autumn SSTA-OGE is a dipole mode), resulting in the continuous heating being pronounced. Meanwhile, thermal diffusion also contributes to forecasting uncertainty and prolongs the SPB duration.

Overall, as compared to SLA-OGEs and SSTA-OGEs, the joint effects of SSTA and SLA act on THA and sea subsurface temperature anomalies, thereby promoting continuous heating and thermal diffusion in the upper ocean [38,39]. This makes both error evolutions and the SPB induced by Joint-OGEs more intense than SLA-OGEs and SSTA-OGEs.

5. Target Observation Sensitive Area Identification

Recently, the validity of the OGE-type initial error as a sensitive area for conducting intensive observations has been confirmed [16]. According to the spatial structures of OGEs in Section 4.1, sensitive areas determined by the Joint-OGEs of SSTA are mainly concentrated in the central-eastern Pacific Ocean, and those of SLA cover almost the entire tropical Pacific Ocean. Despite possible increases in prediction accuracy observed from conducting intensive observations in the abovementioned sensitive areas, it also tremendously raises observation costs. Hence, we propose an effective economic observation network by quantifying the crucial dynamics contributions of Joint-OGEs.

In this trial, Joint-OGEs with different scales are divided into one control group and eight experimental groups. Concretely, the entire areas of Joint-OGEs are referred to as the control group. After erasing weak signals in Joint-OGEs, the core areas of Joint-OGEs are set as the experimental group (Exp. 1), which contains the areas within the absolute isoline of 0.1° in the SSTA and 0.03 m in the SLA for Joint-OGEs. In addition, we also set 90–30% of the core areas as experimental groups (Exp. 2–7), and the corresponding absolute isoline settings are listed in Table 2. To measure the contribution of Joint-OGEs in different scales on the predicted error, we perform the observing system simulation experiments of two reference states with superimposing various initial errors from control and experimental groups. When the predicted error of the experimental group exceeds 60% of the control group, the area involved in the specific experimental group is the best (economic) targeted observation area.

Table 2. The absolute isoline setting for control and experimental groups.

	Absolute Isoline (SSTA(°C)/SLA(m))			
	Summer	Autumn	Winter	Spring
Control group	Entire areas of Joint-OGEs			
Core area (Exp. 1)	0.1/0.003			
90% of core area (Exp. 2)	0.125/0.0332	0.1185/0.03112	0.1109/0.03216	0.113/0.0333
80% of core area (Exp. 3)	0.1487/0.0367	0.134/0.03275	0.1245/0.03485	0.127/0.0372
70% of core area (Exp. 4)	0.1806/0.0403	0.156/0.03453	0.143/0.0376	0.142/0.0415
60% of core area (Exp. 5)	0.2173/0.0459	0.1825/0.03678	0.1689/0.0408	0.1662/0.0479
50% of core area (Exp. 6)	0.255/0.0521	0.216/0.03912	0.204/0.0438	0.2026/0.0548
40% of core area (Exp. 7)	0.3055/0.05915	0.25/0.042	0.243/0.0474	0.25405/0.062
30% of core area (Exp. 8)	0.4102/0.06928	0.36/0.04453	0.3235/0.0523	0.381/0.0708

Figure 14 displays the prediction errors for the El Niño reference state, superimposing varying seasonal Joint-OGEs from the control and experimental groups over 12 months.

Accordingly, at the beginning of the integration, there are small prediction error differences between the control and experimental groups. Further, with increasing predictive time, the difference gradually rises, which may be because the error accumulation induced by the areas beyond the experimental groups resulted in instability in the ocean state.

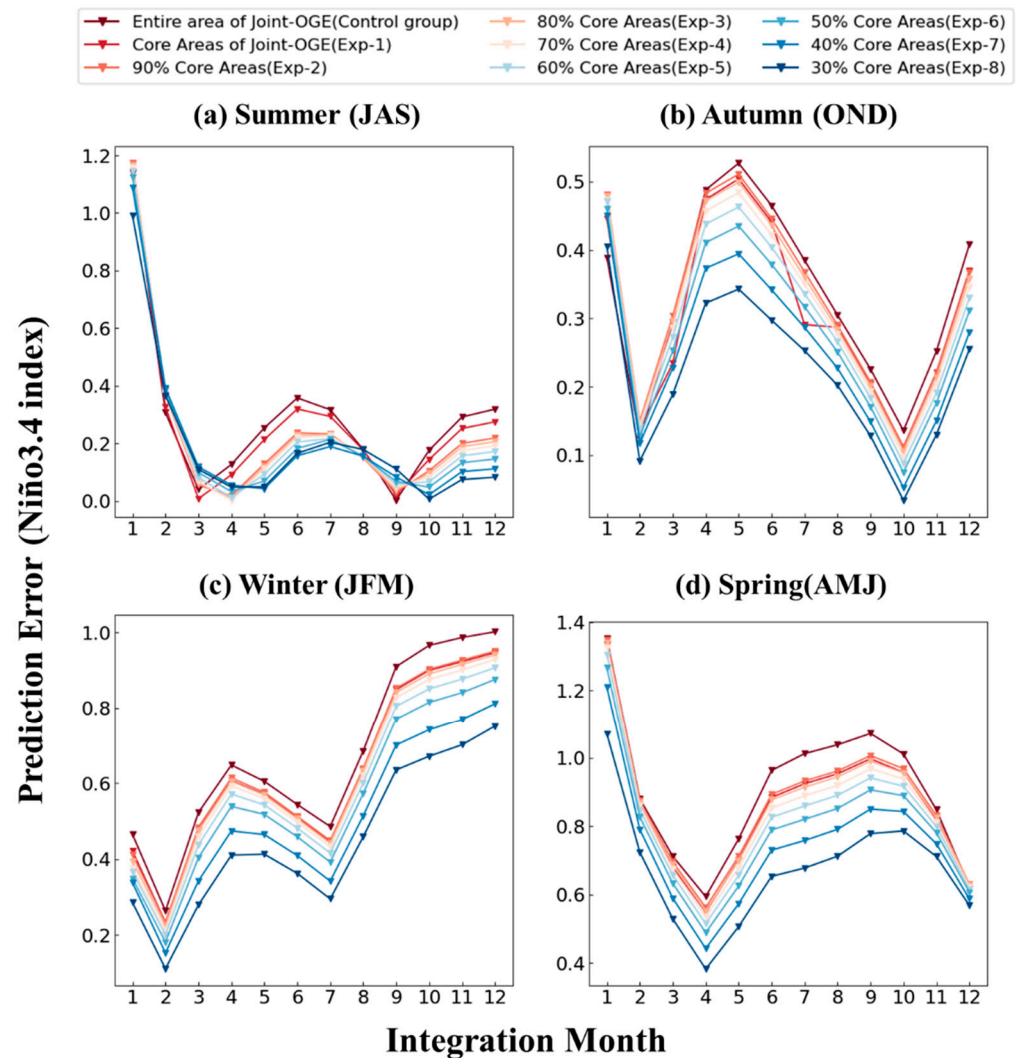


Figure 14. The prediction errors in the Niño3.4 index ($^{\circ}\text{C}$) of every month for El Niño reference state with superimposing varying seasonal Joint–OGEs from control and experimental groups over 12 months.

From differences in forecast errors between the control and experimental groups, appropriate sensitive areas vary with different forecast start seasons. The forecast error can be effectively eliminated by conducting intensive observations in 30% of the core area for forecasts starting from summer, and in the 50% core area for forecasts starting from autumn, winter and spring. Hence, the sensitive areas for different forecast start seasons mainly contain the central-eastern equatorial Pacific and the western and north-eastern tropical Pacific boundary. Furthermore, there is a significant forecast error dropping in 30% and 40% of the core area (Exp. 7, 8) for forecasts starting from autumn, winter and spring, demonstrating that the eastern equatorial Pacific and east-southern tropical Pacific boundary omitted by Exp. 7 and 8 have a crucial role in El Niño forecasting [40].

Figure 15 displays the prediction errors for the La Niña reference state, superimposing varying seasonal Joint–OGEs from the control and experimental groups over 12 months. It

can be found that the difference between the control and experimental groups in forecast error is also initially slight and gradually grows with increasing predictive time.

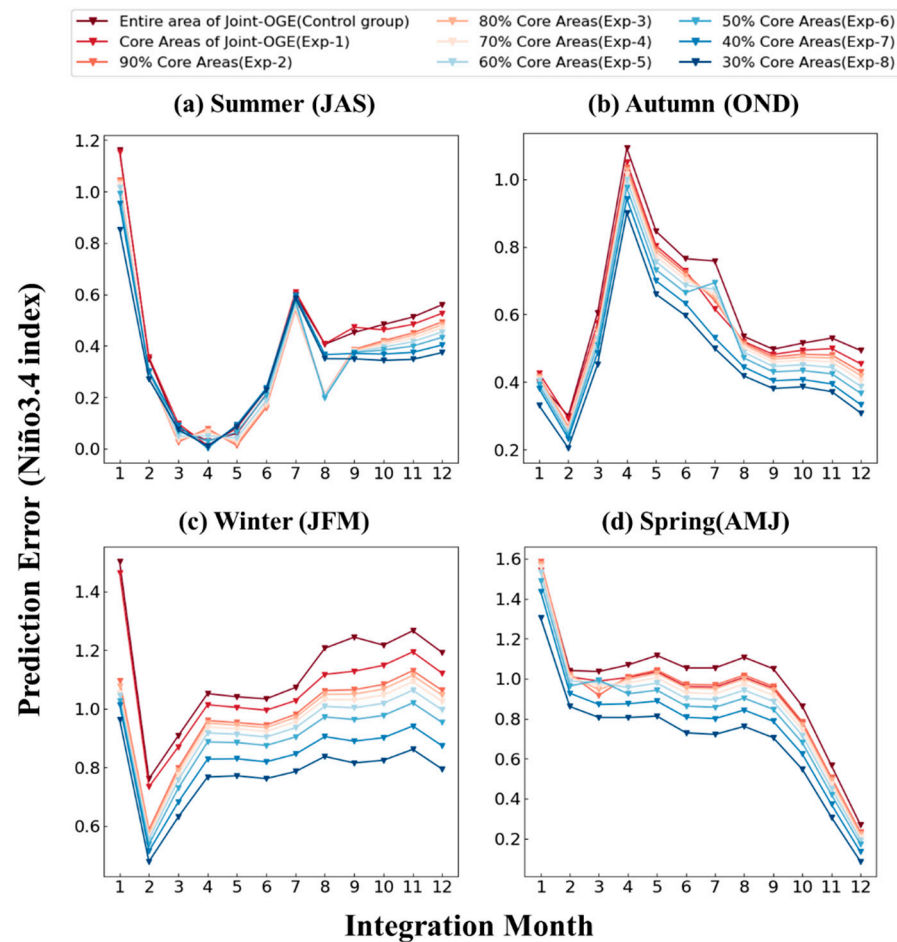


Figure 15. The prediction errors in the Niño3.4 index (°C) of every month for La Niña reference state with superimposing varying seasonal Joint–OGEs from control and experimental groups over 12 months.

Furthermore, when intensive observations are conducted on 30% of the core area (Exp. 8) for forecasts starting from summer, on 50% of the core area (Exp. 6) for forecasts starting from autumn and spring and on 70% of the core areas for winter, forecast errors can be significantly eliminated. Notably, for forecasts starting from winter, the forecast error in 30%, 40% and 50% of the core area (Exp. 6, 7, 8) exhibits noticeable deviation from the control group, which indicates that the west-southern tropical Pacific boundary is a critical area for La Niña forecasting [41].

Even though the best (economic) observation network (sensitive areas) vary depending on the forecast start seasons, universal sensitive areas can be concluded for four seasons through the above experiments. As shown in Figure 16a,b, the sensitive areas of SSTA concentrate in the central-eastern equatorial Pacific. The sensitive areas of SLA are located in the eastern equatorial Pacific and the western and north-eastern tropical Pacific boundary. The universal sensitive areas mentioned above cover approximately 50% of the tropical Pacific Ocean.

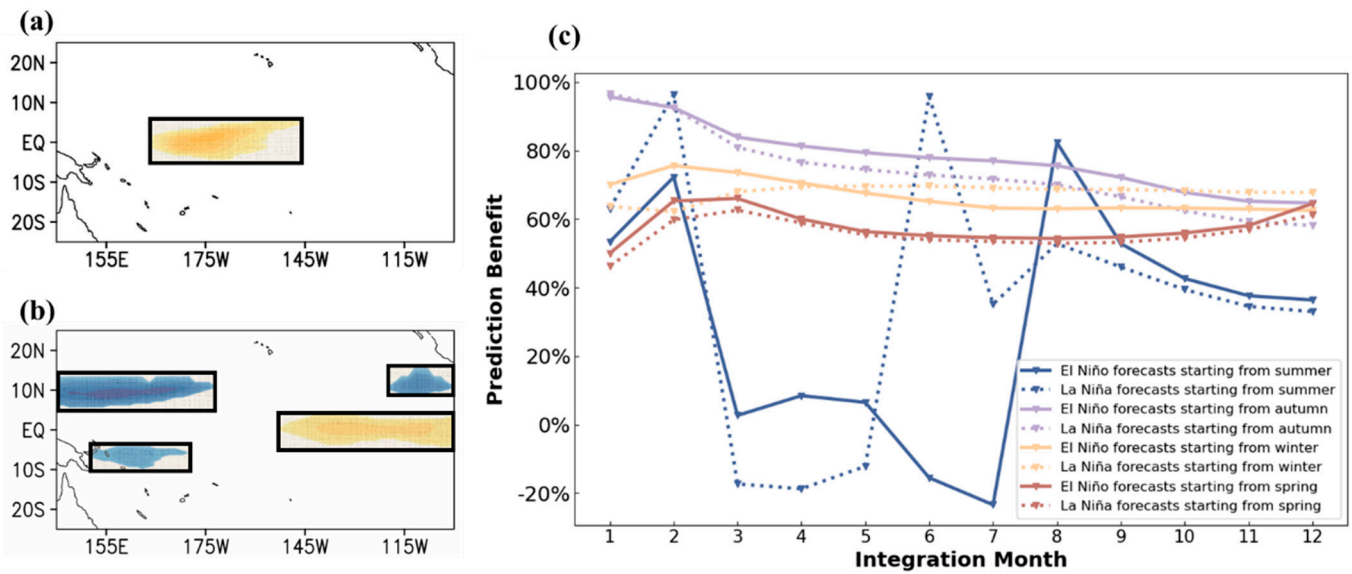


Figure 16. The universal sensitive area identification results for ENSO forecasting. (a,b) illustrate the universal sensitive areas of SSTA and SLA, respectively. In order to evaluate the effectiveness of the above sensitive areas, (c) displays the prediction benefit of removing the Joint–OGEs in the universal sensitive areas for two reference states.

Moreover, through a reduction in the prediction error after removing Joint-OGEs in specific sensitive areas, we measure the prediction benefit of effective observations in universal sensitive areas for improving the forecast results. The benefit is calculated using Equation (7).

$$B_{pred} = \frac{|Ni\tilde{no}3.4_k^{Joint-OG E} - Ni\tilde{no}3.4_k^{ref}| - |Ni\tilde{no}3.4_k^{remove} - Ni\tilde{no}3.4_k^{ref}|}{|Ni\tilde{no}3.4_k^{Joint-OG E} - Ni\tilde{no}3.4_k^{ref}|} \times 100\% \quad (7)$$

The B_{pred} represents the degree of reduction in prediction errors after implementing target observation in universal sensitive areas. As shown in Figure 16a,c, $Ni\tilde{no}3.4_k^{Joint-OG E}$ and $Ni\tilde{no}3.4_k^{ref}$, respectively, represent the prediction results after integrating ICM for k months, with and without superimposed Joint-OGEs on the initial field of the El Niño/La Niña reference state, and $Ni\tilde{no}3.4_k^{remove}$ represents the prediction results removing Joint-OGEs in universal sensitive areas from $Ni\tilde{no}3.4_k^{Joint-OG E}$.

The prediction benefits for different forecasts starting from four seasons in two reference states are shown in Figure 16c. The results demonstrate that if the initial error of Joint-OGEs in universal sensitive areas is eliminated, the prediction errors of ENSO can be reduced efficiently, especially the average prediction benefit starting from the autumn, winter and spring, which can reach more than 66.57%. The exception occurs in the summer, which shows negative benefits during the leading 3–7 months. Since the sensitive areas for summer are relatively small, evidence shows that additional observations in non-sensitive areas may not be beneficial in weakening the SPB and may even strengthen the forecast error [16]. Nevertheless, the average benefits of seasonal forecast still reach 58.31%. Meanwhile, the prediction benefit starting from summer exhibits a stable tendency over the leading 8 months, which also confirms the validity of the universal sensitive areas in long-term ENSO forecasting.

The universal sensitive areas shown in Figure 16a,b are consistent with the conclusions of Duan and Hu [42], Tao et al. [16] and Shin et al. [43] in previous studies. Duan and Hu emphasized the importance of subsurface signals in the western Pacific for ENSO predictions, which can influence the surface through equatorial waves and thermodynamic effects. Tao et al. indicated that the initial states in the central and eastern equatorial Pacific

are essential to effectively improve El Niño prediction skills. Shin et al. proposed that intensive observations of SSH in the eastern and western equatorial Pacific boundary and eastern equatorial Pacific are necessary, especially in extreme ENSO forecasting.

6. Conclusions

In this paper, we explored the error evolutions for the joint effects of SSTA and SLA on growth dynamics and seasonal predictability barriers from the perspective of OGE based on the ICM and CNOP methods. The crucial contributions and conclusions can be summarized as follows:

1. We obtained a wide variety of OGE patterns. In addition to covering almost all the OGE modes obtained by previous studies, there are also extended OGE modes with more detailed information. Various OGEs have varying seasonal dependence and distinct effects on ENSO evolutions and the SPB.

From the spatial structures of OGEs, SSTA-OGEs exhibit seasonal dependence, Joint-OGEs have less, but SLA-OGEs have no seasonal dependence. Moreover, both SSTA-OGEs and Joint-OGEs have seasonal effects on ENSO evolutions. Concretely, the summer and spring SSTA-OGEs lead to overestimating El Niño events and underestimating La Niña events (and vice versa for autumn and winter SSTA-OGEs). Meanwhile, all seasonal Joint-OGEs induce an overestimation of the El Niño events and underestimation of the La Niña events. From error evolutions and the resulting SPB, both SSTA-OGEs and Joint-OGEs result in obvious error evolutions and the SPB but Joint-OGEs with more intensity than SSTA-OGEs. In addition, SLA-OGEs have almost no impact on ENSO evolutions;

2. By analyzing the mechanism of OGE evolutions and the SPB, we found that the principal physical processes involved in OGE evolutions also govern the SPB, which, induced by SSTA-OGEs, is mainly owing to Bjerknes feedback. For Joint-OGEs, the SPB is primarily due to the continuous heating between the upper ocean and the thermal diffusion in response to the discharge process.

We demonstrate that the joint effects of SSTA and SLA have a significant impact on error evolutions and the SPB. Both error evolutions and the SPB induced by Joint-OGEs are more intense than SSTA-OGEs and SLA-OGEs, indicating that THA represented by SLA reconstructs the vertical convection in the upper ocean and contributes significantly to SSTA evolution. Meanwhile, the sea subsurface temperature anomalies influenced by SLA [34] accelerate the thermal dissipation to mid-latitudes in response to the discharge process, which is a dynamical detail ignored by previous studies of the univariate optimal initial errors.

3. Based on the Joint-OGE patterns, our observation scheme proposals include not only the most (economically) sensitive area schemes for each forecast starting from different seasons but also generic multivariate observation schemes. In detail, generic sensitive areas encompass the central-eastern equatorial Pacific and the western and north-eastern tropical Pacific boundary, where conducting intensive observation contributes to the ENSO prediction benefits, reaching 58.31% on average.

Many endeavors have previously been made to explore the OGEs of ENSO based on the CNOP approach. The OGE modes obtained in this paper cover almost all the SSTA patterns determined by previous studies. Precisely, Mu et al. [44] identified seasonal OGEs according to adjoint methods and the CNOP approach in the ZC model, whose spatial structures are similar to seasonal SSTA-OGEs (Figure 6) (only the summer mode sees the opposite phase). Tao et al. [14] also calculated OGEs using an adjoint method and investigated the seasonal OGEs in ICM; all of them have negative SSTA errors in the equatorial central Pacific, which was somewhat consistent with the winter mode of SSTA-OGE (Figure 6c). Similarly, our OGE patterns also corresponded to non-seasonal OGEs [45,46]. In particular, Xu et al. [28] obtained three types of OGEs with distinct El Niño events in CESM, which were somewhat similar to the winter mode of SSTA-OGE (Figure 6c), autumn mode of Joint-OGE (Figure 8b) and spring mode of Joint-OGE (Figure 8d). The

comprehensive OGE patterns imply the validity of our experimental methods and are reliable and valuable supports for dynamic analyses.

This study aims to examine the error evolution of the joint effects of SST and SL induced by the initial perturbation on ENSO predictions. However, extensive evidence has suggested that there are still many variates that also play an essential role in influencing ENSO events. For example, Zheng and Zhu [47] used the ICM to show that the SST prediction errors were reduced by improving the simulation of the zonal wind stress anomalies. The salinity is also an essential factor in the oceanic evolution from seasonal to interannual timescales; its interannual variations significantly affect the density and mixed layers of the central and western tropical Pacific, thus affecting the sea temperature and the development of ENSO. Geng T, et al. [48] found that changes in atmospheric convection significantly impact the ENSO asymmetry. Thus, further exploration will focus on more physical variables, researching the joint variable mechanisms in ENSO predictability. In addition, identifying the OPR, OGE and corresponding sensitive areas is also essential for target observations. The observation network can be refined to explore ENSO and advance the scientific understanding of its causes. Furthermore, a real-time observation system can be established based on multivariate predictability research, which can strengthen the adoption of target observational sensitive areas, supporting prediction systems for the ocean, weather and climate services.

Author Contributions: Conceptualization, B.M., X.Q., S.Y. and B.Q.; methodology, X.Q.; software, X.Q.; validation, X.Q.; formal analysis, B.M., X.Q., S.Y. and B.Q.; investigation, B.M., X.Q., S.Y. and B.Q.; resources, X.Q.; writing—original draft preparation, B.M., X.Q., S.Y. and B.Q.; writing—review and editing, B.M., X.Q., S.Y. and B.Q.; visualization, X.Q.; supervision, B.M., X.Q., S.Y. and B.Q.; project administration, B.M., X.Q., S.Y. and B.Q.; funding acquisition, B.M. and S.Y. All authors have read and agreed to the published version of the manuscript.

Funding: This study is supported in part by the Meteorological Joint Funds of the National Natural Science Foundation of China (under Grant U2142211), in part by the Key Project Fund of Shanghai 2020 “Science and Technology Innovation Action Plan” for Social Development (under Grant 20dz1200702), in part by the National Key Research and Development Program of China (under Grant 2020YFA0608000), in part by the National Natural Science Foundation of China (under Grant 42075141) and, in part by the first batch of Model Interdisciplinary Joint Research Projects of Tongji University in 2021 (under Grant YB-21-202110).

Institutional Review Board Statement: Not applicable.

Informed Consent Statement: Not applicable.

Data Availability Statement: The data presented in this study will be available to the researchers upon request.

Conflicts of Interest: The authors declare no conflict of interest.

Appendix A

Table A1. List of acronyms involved in this article along with their brief descriptions.

No.	Term	Description
1	ENSO data	The El Niño–Southern Oscillation
2	Niño3.4 index	mean of SST anomalies in the Niño 3.4 region (120° W–170° W, 5° N–5° S)
3	IOCAS ICM	an intermediate coupled model developed at the Institute of Oceanology, Chinese Academy of Sciences
4	CNOP	conditional nonlinear optimal perturbation
5	PB	predictability barrier
6	SPB	spring predictability barrier
7	OGE	the optimal growth initial error
8	OPR	the optimal precursor

Table A1. Cont.

No.	Term	Description
9	SSTA	sea surface temperature anomalies
10	SLA	sea level anomalies
11	THA	thermocline height anomalies
12	T_e	the temperature of subsurface water entrained into the mixed layer
13	Z_{20}	20 °C depth anomalies
14	SLA-OGE	the optimal growth initial error of SLA
15	SSTA-OGE	the optimal growth initial error of SSTA
16	Joint-OGE	the optimal growth initial error of SSTA and SLA
17	GD	gradient definition algorithm
18	ZC model	Zebiak–Cane model
19	MM5	Mesoscale Model fifth Generation

References

- Rasmusson, E.M.; Carpenter, T.H. Variations in tropical sea surface temperature and surface wind fields associated with the Southern Oscillation/El Niño. *Mon. Weather Rev.* **1982**, *110*, 354–384. [[CrossRef](#)]
- Philander, S.G.H. El Niño southern oscillation phenomena. *Nature* **1983**, *302*, 295–301. [[CrossRef](#)]
- Wyrtki, K. El Niño—The dynamic response of the equatorial Pacific Ocean to atmospheric forcing. *J. Phys. Oceanogr.* **1975**, *5*, 572–584. [[CrossRef](#)]
- Chen, D.; Cane, M.A.; Kaplan, A.; Zebiak, S.E.; Huang, D. Predictability of El Niño over the past 148 years. *Nature* **2004**, *428*, 733–736. [[CrossRef](#)]
- Beobide-Arsuaga, G.; Bayr, T.; Reintges, A.; Latif, M. Uncertainty of ENSO-amplitude projections in CMIP5 and CMIP6 models. *Clim. Dyn.* **2021**, *56*, 3875–3888. [[CrossRef](#)]
- Available online: <https://iri.columbia.edu/our-expertise/climate/forecasts/enso/current/> (accessed on 20 October 2022).
- Fang, X.; Xie, R. A brief review of ENSO theories and prediction. *Sci. China Earth Sci.* **2020**, *63*, 476–491. [[CrossRef](#)]
- Liu, Z.; Jin, Y.; Rong, X. A theory for the seasonal predictability barrier: Threshold, timing, and intensity. *J. Clim.* **2019**, *32*, 423–443. [[CrossRef](#)]
- Zhang, R.H.; Zebiak, S.E.; Kleeman, R.; Keenlyside, N. A new intermediate coupled model for El Niño simulation and prediction. *Geophys. Res. Lett.* **2003**, *30*. [[CrossRef](#)]
- Zhang, R.H.; Gao, C. The IOCAS intermediate coupled model (IOCAS ICM) and its real-time predictions of the 2015–2016 El Niño event. *Sci. Bull.* **2016**, *61*, 1061–1070. [[CrossRef](#)]
- Zhang, R.H.; Tao, L.J.; Gao, C. An improved simulation of the 2015 El Niño event by optimally correcting the initial conditions and model parameters in an intermediate coupled model. *Clim. Dyn.* **2018**, *51*, 269–282. [[CrossRef](#)]
- Gao, C.; Chen, M.; Zhou, L.; Feng, L.; Zhang, R.H. The 2020–2021 prolonged La Niña evolution in the tropical Pacific. *Sci. China Earth Sci.* **2022**, *65*, 2248–2266. [[CrossRef](#)]
- Zhang, R.H.; Gao, C.; Feng, L. Recent ENSO evolution and its real-time prediction challenges. *Natl. Sci. Rev.* **2022**, *9*, nwac052. [[CrossRef](#)] [[PubMed](#)]
- Tao, L.J.; Zhang, R.H.; Gao, C. Initial error-induced optimal perturbations in ENSO predictions, as derived from an intermediate coupled model. *Adv. Atmos. Sci.* **2017**, *34*, 791–803. [[CrossRef](#)]
- Chen, H.; Wang, Q.; Zhang, R.H. Sensitivity of El Niño diversity prediction to parameters in an intermediate coupled model. *Clim. Dyn.* **2023**, 1–18. [[CrossRef](#)]
- Tao, L.J.; Gao, C.; Zhang, R.H. ENSO predictions in an intermediate coupled model influenced by removing initial condition errors in sensitive areas: A target observation perspective. *Adv. Atmos. Sci.* **2018**, *35*, 853–867. [[CrossRef](#)]
- Tian, B.; Ren, H.L. Diagnosing SST Error Growth during ENSO Developing Phase in the BCC_CSM_{1.1}(m) Prediction System. *Adv. Atmos. Sci.* **2022**, *39*, 427–442. [[CrossRef](#)]
- Lee, J.; Planton, Y.Y.; Gleckler, P.J.; Sperber, K.R.; Guilyardi, E.; Wittenberg, A.T.; McPhaden, M.J.; Pallotta, G. Robust evaluation of ENSO in climate models: How many ensemble members are needed? *Geophys. Res. Lett.* **2021**, *48*, e2021GL095041. [[CrossRef](#)]
- Zhou, Q.; Chen, L.; Duan, W.; Wang, X.; Zu, Z.; Li, X.; Zhang, S.; Zhang, Y. Using conditional nonlinear optimal perturbation to generate initial perturbations in ENSO ensemble forecasts. *Weather Forecast.* **2021**, *36*, 2101–2111. [[CrossRef](#)]
- L’Heureux, M.L.; Levine, A.F.; Newman, M.; Ganter, C.; Luo, J.J.; Tippett, M.K.; Stockdale, T.N. ENSO prediction. *El Niño South. Oscil. A Chang. Clim.* **2020**, 227–246.
- Hu, J.; Duan, W.; Zhou, Q. Season-dependent predictability and error growth dynamics for La Niña predictions. *Clim. Dyn.* **2019**, *53*, 1063–1076. [[CrossRef](#)]
- Duan, W.; Liu, X.; Zhu, K.; Mu, M. Exploring the initial errors that cause a significant “spring predictability barrier” for El Niño events. *J. Geophys. Res. Ocean.* **2009**, 114. [[CrossRef](#)]

23. Mu, M.; Zhou, F.; Wang, H. A method for identifying the sensitive areas in targeted observations for tropical cyclone prediction: Conditional nonlinear optimal perturbation. *Mon. Weather Rev.* **2009**, *137*, 1623–1639. [[CrossRef](#)]
24. Mu, B.; Cui, Y.; Yuan, S.; Qin, B. Simulation, precursor analysis and targeted observation sensitive area identification for two types of ENSO using ENSO-MC v1.0. *Geosci. Model Dev.* **2022**, *15*, 4105–4127. [[CrossRef](#)]
25. Zhang, J.; Hu, S.; Duan, W. On the sensitive areas for targeted observations in ENSO forecasting. *Atmos. Ocean. Sci. Lett.* **2021**, *14*, 100054. [[CrossRef](#)]
26. Mu, M.; Duan, W.S.; Wang, B. Conditional nonlinear optimal perturbation and its applications. *Nonlinear Process. Geophys.* **2003**, *10*, 493–501. [[CrossRef](#)]
27. Mu, M.; Yu, Y.; Xu, H.; Gong, T. Similarities between optimal precursors for ENSO events and optimally growing initial errors in El Niño predictions. *Theor. Appl. Climatol.* **2014**, *115*, 461–469. [[CrossRef](#)]
28. Xu, H.; Chen, L.; Duan, W. Optimally growing initial errors of El Niño events in the CESM. *Clim. Dyn.* **2021**, *56*, 3797–3815. [[CrossRef](#)]
29. Yang, Z.; Fang, X.; Mu, M. Optimal Precursors for Central Pacific El Niño Events in GFDL CM2p1. *J. Clim.* **2023**, 1–30. [[CrossRef](#)]
30. Mu, B.; Ren, J.; Yuan, S.; Zhang, R.H.; Chen, L.; Gao, C. The optimal precursors for ENSO events depicted using the gradient-definition-based method in an intermediate coupled model. *Adv. Atmos. Sci.* **2019**, *36*, 1381–1392. [[CrossRef](#)]
31. Bjerknes, J. Atmospheric teleconnections from the equatorial Pacific. *Mon. Weather Rev.* **1969**, *97*, 163–172. [[CrossRef](#)]
32. Neelin, J.D.; Battisti, D.S.; Hirst, A.C.; Jin, F.F.; Wakata, Y.; Yamagata, T.; Zebiak, S.E. ENSO theory. *J. Geophys. Res. Ocean.* **1998**, *103*, 14261–14290. [[CrossRef](#)]
33. Zelle, H.; Appeldoorn, G.; Burgers, G.; van Oldenborgh, G.J. The relationship between sea surface temperature and thermocline depth in the eastern equatorial Pacific. *J. Phys. Oceanogr.* **2004**, *34*, 643–655. [[CrossRef](#)]
34. Meinen, C.S.; McPhaden, M.J. Observations of warm water volume changes in the equatorial Pacific and their relationship to El Niño and La Niña. *J. Clim.* **2000**, *13*, 3551–3559. [[CrossRef](#)]
35. Keenlyside, N.; Kleeman, R. Annual cycle of equatorial zonal currents in the Pacific. *J. Geophys. Res. Ocean.* **2002**, *107*, 8-1–8-13. [[CrossRef](#)]
36. Mu, B.; Ren, J.; Yuan, S. An efficient approach based on the gradient definition for solving conditional nonlinear optimal perturbation. *Math. Probl. Eng.* **2017**, *2017*, 3208431. [[CrossRef](#)]
37. Mu, B.; Ren, J.; Yuan, S.; Zhou, F. Identifying typhoon targeted observations sensitive areas using the gradient definition based method. *Asia-Pac. J. Atmos. Sci.* **2019**, *55*, 195–207. [[CrossRef](#)]
38. Li, X.; Hu, Z.Z.; Zhao, S.; Ding, R.; Zhang, B. On the asymmetry of the tropical Pacific thermocline fluctuation associated with ENSO recharge and discharge. *Geophys. Res. Lett.* **2022**, *49*, e2022GL099242. [[CrossRef](#)]
39. O’Kane, T.J.; Squire, D.T.; Sandery, P.A.; Kitsios, V.; Matear, R.J.; Moore, T.S.; Risbey, J.S.; Watterson, I.G. Enhanced ENSO prediction via augmentation of multimodel ensembles with initial thermocline perturbations. *J. Clim.* **2020**, *33*, 2281–2293. [[CrossRef](#)]
40. Zhao, S.; Jin, F.F.; Long, X.; Cane, M.A. On the breakdown of ENSO’s relationship with thermocline depth in the central-equatorial Pacific. *Geophys. Res. Lett.* **2021**, *48*, e2020GL092335. [[CrossRef](#)]
41. Zhao, Y.; Di Lorenzo, E. The impacts of extra-tropical ENSO precursors on tropical Pacific decadal-scale variability. *Sci. Rep.* **2020**, *10*, 3031. [[CrossRef](#)]
42. Duan, W.; Hu, J. The initial errors that induce a significant “spring predictability barrier” for El Niño events and their implications for target observation: Results from an earth system model. *Clim. Dyn.* **2016**, *46*, 3599–3615. [[CrossRef](#)]
43. Shin, S.I.; Sardeshmukh, P.D.; Newman, M.; Penland, C.; Alexander, M.A. Impact of annual cycle on ENSO variability and predictability. *J. Clim.* **2021**, *34*, 171–193. [[CrossRef](#)]
44. Mu, M.; Xu, H.; Duan, W. A kind of initial errors related to “spring predictability barrier” for El Niño events in Zebiak-Cane model. *Geophys. Res. Lett.* **2007**, *34*. [[CrossRef](#)]
45. Yu, Y.; Duan, W.; Xu, H.; Mu, M. Dynamics of nonlinear error growth and season-dependent predictability of El Niño events in the Zebiak-Cane model. *Q. J. R. Meteorol. Soc. A J. Atmos. Sci. Appl. Meteorol. Phys. Oceanogr.* **2009**, *135*, 2146–2160. [[CrossRef](#)]
46. Duan, W.; Wei, C. The ‘spring predictability barrier’ for ENSO predictions and its possible mechanism: Results from a fully coupled model. *Int. J. Climatol.* **2013**, *33*, 1280–1292. [[CrossRef](#)]
47. Zheng, F.; Zhu, J. Coupled assimilation for an intermediated coupled ENSO prediction model. *Ocean Dyn.* **2010**, *60*, 1061–1073. [[CrossRef](#)]
48. Geng, T.; Cai, W.; Wu, L.; Yang, Y. Atmospheric convection dominates genesis of ENSO asymmetry. *Geophys. Res. Lett.* **2019**, *46*, 8387–8396. [[CrossRef](#)]

Disclaimer/Publisher’s Note: The statements, opinions and data contained in all publications are solely those of the individual author(s) and contributor(s) and not of MDPI and/or the editor(s). MDPI and/or the editor(s) disclaim responsibility for any injury to people or property resulting from any ideas, methods, instructions or products referred to in the content.